Integrated Computational Measurement System for Enhanced Polarimetric Measurements

by

Shahid Abbas Haider

A thesis
presented to the University of Waterloo
in fulfillment of the
thesis requirement for the degree of
Master of Applied Sciences
in
Systems Design Engineering

Waterloo, Ontario, Canada, 2015

I hereby declare that I am the sole author of this thesis. This is a true copy of the thesis, including any required final revisions, as accepted by my examiners.

I understand that my thesis may be made electronically available to the public.

Abstract

Polarimetry is an useful tool in chemical identification and characterisation both inside and outside the lab. It is a modality where the effects of chiral molecules, water impurities and cancerous cells are noticeable through changes in light polarisation as it passes through these samples. In the case of chiral molecules, like glucose, this change in polarisation manifests as a rotation in polarisation. The amount of rotation that occurs is governed by Boits Law; however, without large optical path lengths, or high concentrations of solution, these rotations are typically very small, requiring elaborate, large and costly apparatus. These devices ensure accuracy by performing complex optical procedures or time-averaging point measurements. This ensures that any intensity variation in the measurements is a result of rotation and not from inherent error in the system or from noise, such as sensor or shot noise. Time Averaging is a lengthy process and does not utilizes all the information from the incident light beam. To this end, we propose, design and build a novel inexpensive, compact computational polarimetric measurement system. This system computationally enhances polarimetric measurements by utilising the full spot size observed on a spatial detector array. This allows the system to need only a single acquisition to enhance the polarimetric measurements by recognizing that the full CMOS detector is a spatial array of photosensitive areas. By using the full spot, it can mimic temporal acquisitions, but through space rather than time. To ensure accuracy in computational enhancement, detector noise and system error are characterized for their effect on both pixel intensity and polarimetric measurement accuracy, given the entire acquisition system. All the while, this device achieves a spatial footprint of less than 245 cm^3 and costs 68% less than the state-of-the-art lab polarimeters.

Two experiments are performed to validate this system. The first experiment is a synthetic experiment meant to demonstrate the performance and robustness of this device in determining the concentration of chiral molecules in a solution. The second experiment validates the real life capability of this system by determining the concentration of Maltodextrin in water. Through these experiments, it is shown that the spatial enhancement methods are capable of improving the estimate of chiral molecule concentrations. We also demonstrate that through the use of a model based spatial enhancement method, we can estimate with more accuracy and precision than the state-of-the-art enhancement method of Temporal Averaging.

This system demonstrates that an inexpensive, compact polarimetry device can report accurate measurements of chiral molecule concentrations through *a priori* knowledge of the imperfections in the optical elements used and through computational enhancement methods that utilise the entire light beam's spot incident on a spatial detector array. This

system acts as a proof of concept that the polarimetry modality can be taken outside the lab and into the field for chiral molecule concentration identification. It also demonstrates that spatial enhancement methods can be used for polarimetric measurement enhancement, potentially reducing overall acquisition time which is advantageous in dynamic conditions.

Acknowledgements

I would like to thank everyone who assisted and encouraged me during the time I was writing my thesis. I would like to thank the following people in particular:

- Prof. Alexander Wong and Farnoud Kazemzadeh. They were my personal and academic mentors and have taught me never to rush into things before considering all the options.
- Prof. David Clausi for being my mentor and providing me with important advice for my future academic and professional careers.
- Prof. Maud Gorbet and Sara Molladavoodi for assisting me in the wet lab work, which was necessary to perform the real experiments.

Dedication

This thesis is dedicated to my loving and caring family. They are the people in my life that have encouraged and supported me through my ups and downs and this thesis is written proof of their efforts.

Table of Contents

List of Tables

List of Figures

List of Symbols

α	Scaling parameter for Model Fitting
$\cdot$	Dot product between two vectors
η	Value sampled from a zero-mean Gaussian distribution
$\hat{\mathcal{U}}$	Enhanced set of measurements that will be similar to the ideal intensity measurements of the polarised state of the light beam
λ	The wavelength of a wave
$[\alpha]_\lambda^T$	Specific rotation for a chiral molecule, defined at a particular wavelength λ and temperature T
$\mathcal{C}$	Cost function for Model Fitting
$\mathcal{E}$	Some set of error values
$\mathcal{I}$	The set of ideal intensities when there are no intensity variations in the system
$\mathcal{L}$	Set of measurements to represent the ideal laser spot incident on the detector
$\mathcal{N}_i$	The spatial neighbourhood about pixel i
$\mathcal{P}_\lambda(n)$	The Poisson distribution which models the probability of n events occurring given a rate of occurrence of λ
$\mathcal{U}$	The set of observed intensities on a detector
ω	The angular frequency of a wave
$\|\cdot\|$	Magnitude of a vector

ϕ	Phase delay difference between the orthogonal wave components, $\phi_y - \phi_x$
ϕ_i	Phase delay in the wave propagation in direction $i = \{x, y\}$
τ	Single variable representation of the wave propagator in the z direction, $\omega t - kz$
$\mathbf{k}$	The wave vector of a wave
$\mathbf{r}$	Vector representation of some point in 3-space
θ	Rotation in linearly polarised light
$\underline{\theta}$	Parameter set for Model Fitting
C	Intensity bias parameter for Model Fitting
E_i	The wave amplitude in the $i = \{x, y, z\}$ orthogonal directions
$E_{o\{i\}}$	The maximum wave amplitude in the $i = \{x, y, z\}$ orthogonal directions
p_p	Scaling factor parallel to the polarising direction
p_s	Scaling factor cross (perpendicular) to the polarising direction
t	Variable representation of time
x, y, z	Co-ordinates to represent spatial location in Cartesian three-space

Chapter 1

Introduction

Light is an amazing thing. The changes that light undergoes as it passes through matter can tell you a lot about that matter's characteristics. For example, the matter's chemical make up can absorb or scatter different wavelengths and if those wavelengths are known *a priori*, then its' chemical composition can be identified. A research field to measure and analyse this spectral change in light is called 'spectroscopy.'

Another change that light can undergo is a phase or amplitude change between the orthogonal components of the light wave, i.e., a change in the polarisation. Figure 1.1 shows examples of polarised light waves (explained further in Chapter 2). This phase and amplitude change can occur due to an anisotropy in material structure or from matter inhomogeneity. Measuring and studying this change in light polarisation is called 'polarimetry.'

Polarimetry has been shown to be capable in flow cytometry, bacteria identification [2, 3], cancer detection [4, 5, 6, 7], and measuring sugar concentration [8, 9, 10], to cite a few examples. These applications make it worthwhile to explore ways to measure the polarisation state of light as it scatters through matter.

1.1 Measuring Polarisation State

To describe the polarised state of light, devices look to measure the complete polarisation state of light by measuring its' four Stokes parameters. These four parameters are explained in further detail in Chapter 2. Devices that measure Stokes parameters can be split into two categories: wavefront and amplitude division devices.

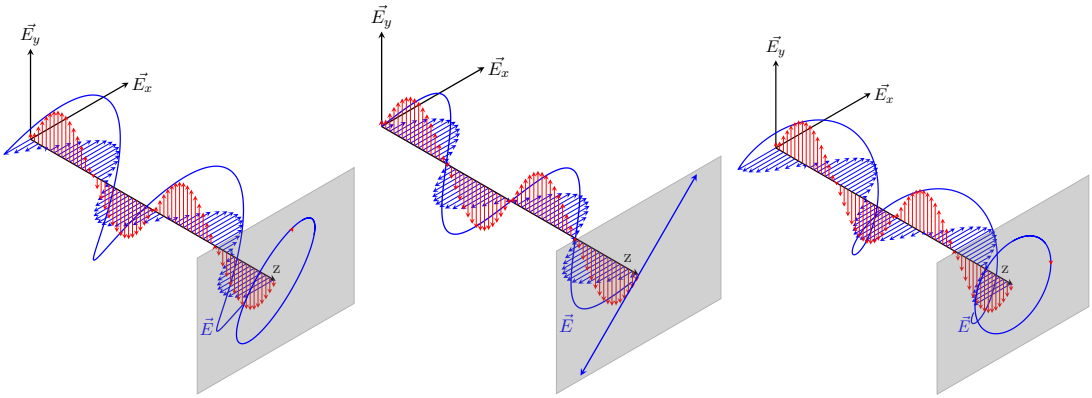

(a) Elliptical polarisation (b) Linear polarisation (c) Circular polarisation

Figure 1.1: Examples of polarised light [1].

Amplitude division devices take the entire energy of the wave and split it to measure the Stokes parameters. This is the common method employed by industrial optical lab and chemical lab polarimeters. For example, the PAX5720 line of polarimeters from Thorlabs (Thorlabs, NJ) or with MCP-Polarimeters from Anton-Paar (Anton-Paar Germany GmbH, Germany) use amplitude division methods. Wavefront division devices split the wavefront of light and, under the assumption that the polarisation of the wave is consistent across the wavefront area being measured, measure the polarisation state. For example, micropolariser arrays where polarisation state measurement is on the pixel level [11, 12, 13, 14, 15] are wavefront division devices. Wavefront division devices are still young in their development, and while performing well under collimated light, suffer when imaging due to aberrations and pixel cross talk/diffraction [12, 13].

Most industrial or scientific amplitude division devices are quite large and quite costly. The size and cost are proportional to the accuracy one can expect from these devices due to the quality of the optical elements. For example, the PAX5720 polarimeter, mentioned earlier, is roughly $8000 USD.

1.2 Enhancing Polarimetric Measurements

Stokes parameters are measured through the irradiance of light on photosensitive materials after passing through a set of appropriate filters. Typically, photodiodes or photomultipliers are used as the transducers. These devices work through the photovoltaic effect,

(a) Thorlabs PAX5710IR Polarimeter (b) Anton-Paar Polarimeters

Figure 1.2: Examples of lab and industrial polarimeters.

converting irradiance into a voltage or a current through active sensing areas. The outgoing signal is amplified using operational amplifiers at the read-out electronics.

The photovoltaic effect in these devices can cause noise to occur in the form of dark current and shot noise. Additional noise can arise from the read-out amplifier. The dark current and read-out amplifier noise are modelled as Gaussian distributions and the shot noise is modelled as a Poisson distribution [16].

The noise from these sources can be reduced, thereby enhancing the measurements, in four ways: i) averaging over multiple temporal measurements [17], ii) lock-in amplifiers [18], iii) an increase in photosensitive areas, or iv) by amplifying the potential energy difference.

Multiple measurements over time can be averaged to provide an enhanced measurement under Gaussian noise assumptions. Lock-in amplifiers are capable of amplifying minute signals that exist under the noise floor, but are extremely large and costly. An increase in photosensitive areas decreases noise under the assumption that the overall signal is homogeneous and the mean of the sensing areas is the signal, again, under Gaussian noise assumptions. The increase in sensing areas also allows for a faster measurement of the polarised state. Photomultipliers increase the potential energy difference that occurs from an incident photon thereby suppressing any difference created from other sources.

1.3 Thesis Contributions

The objective of this thesis is to design of an inexpensive, compact polarimetric system that is capable of reporting polarimetric measurements for measuring chiral molecule concentration, thereby overcoming the need for a large, expensive tabletop apparatus.

The contributions of this thesis are

1. An inexpensive, compact polarimetric measurement system for measuring chiral molecule concentration has been built. The design, formulation and analysis of this system is done in Chapter 3.

2. The use of spatial detector arrays to utilise the full spot size on the detector to mimic the capturing of multiple temporal measurements in Chapter 4, Section 4.3.

3. The correction of polarimetric measurement intensity variations that arise from inexpensive optical elements and random measurement uncertainties from noise using spatial computational methods with knowledge of the errors incorporated *a priori*. The formulation of two spatial algorithms is done in Chapter 4.

The results from these contributions are reported and analysed in Chapter 5 and 6. Discussions of future work and conclusions for this system are in Chapter 7.

Chapter 2

Background

This chapter explorew the state-of-the-art in polarimetric system design for measurement enhancement. Theoretical tools and terminology used in polarimetry are introduced in Section 2.1, polarimetric system designs for enhancing measurements are explored in Section 2.2, and post-processing techniques used for noise reduction are discussed in Section 2.3.

2.1 Polarimetric Theory

Polarimetry is the measurement of phase and amplitude differences between orthogonal components in a light wave. These measurements describe a wave's polarisation state. This section will describe the theoretical foundation that describes the polarisation of a light wave, followed by the mathematical tools used in polarimetry. These derivations are summarised from Tuchin *et al.* [2], Goldstein [19], and Collett [20].

2.1.1 Polarised Light

Ignoring diffraction, light can be described as an oscillating, monochromatic electromagnetic (EM) planar wave emitting from a point source with some wavelength λ and angular frequency ω. For the scope of this thesis, the polarisation of non-monochromatic waves will not be described.

If the EM wave is imagined to be travelling in some arbitrary direction through a homogeneous, isotropic medium, $\mathbf{r} = \mathbf{r}(x, y, z)$, then the electric wave's amplitude can be described as

$$E(\mathbf{r}, t) = \mathbf{E_o} \cos(\omega t - \mathbf{k} \cdot \mathbf{r} + \phi_i) \tag{2.1}$$

where $\mathbf{E_o} = \mathbf{E_o}(x, y, z)$ is the maximum amplitude, ϕ_i is some phase delay in the wave, and $\mathbf{k}$ is the wave vector, where $\| \mathbf{k} \| = \frac{2\pi}{\lambda}$. The wave is assumed to be travelling in three-space (x, y, z), allowing for eq. 2.1 to be decomposed into a scalar representation in three orthogonal directions

$$E_x(\mathbf{r}, t) = E_{ox} \cos(\omega t - \mathbf{k} \cdot \mathbf{r} + \phi_x) \tag{2.2}$$

$$E_y(\mathbf{r}, t) = E_{oy} \cos(\omega t - \mathbf{k} \cdot \mathbf{r} + \phi_y) \tag{2.3}$$

$$E_z(\mathbf{r}, t) = E_{oz} \cos(\omega t - \mathbf{k} \cdot \mathbf{r} + \phi_z) \tag{2.4}$$

where E_{ox}, E_{oy}, and E_{oz} are the maximum amplitudes in each of the three orthogonal directions. The term polarisation is actually this vectorial nature of the wave and polarimetry is the measurement of this vectorial nature. For the rest of this thesis, it is assumed that there will be no change in the wave's propagation direction. The propagation direction will be along the z axis and since EM waves are defined as transverse waves in free space, there will only be vibration in the x and y directions for the electric waves, thereby reducing the amplitude equations from eq. 2.2, 2.3, 2.4 to eq. 2.5 and eq. 2.6.

$$E_x(z, t) = E_{ox} \cos(\omega t - kz + \phi_x) \tag{2.5}$$

$$E_y(z, t) = E_{oy} \cos(\omega t - kz + \phi_y) \tag{2.6}$$

The term $\omega t - kz$ can be called the propagator and be represented by τ. Using τ, eq. 2.5 and 2.6 can be rephrased as eq. 2.7 and 2.8 to make the proceeding formulation easier.

$$E_x(z, t) = E_{ox} \cos(\tau + \phi_x) \tag{2.7}$$

$$E_y(z, t) = E_{oy} \cos(\tau + \phi_y) \tag{2.8}$$

These two equations can be combined to form the equation of an ellipse. The term (z, t) will be dropped for the following equations in this section.

$$\frac{E_x^2}{E_{ox}^2} + \frac{E_y^2}{E_{oy}^2} - 2\frac{E_x}{E_{ox}}\frac{E_y}{E_{oy}}\cos\phi = \sin^2\phi \tag{2.9}$$

where the phase delay difference, ϕ, is defined as $\phi = \phi_y - \phi_x$. This derivation demonstrates that the wave generally propagates as an ellipse. This behaviour is coined the optical ellipse while eq. 2.9 is the polarisation ellipse.

Special (Degenerate) forms of the polarisation ellipse can occur, leading to these polarisations: i) E_{oy} or E_{ox} is 0, ii) ϕ is 0 or π, iii) ϕ is $\frac{\pi}{2}$ or $\frac{3\pi}{2}$, and iv) $E_{oy} = E_{ox} = E_o$ and $\phi = \frac{\pi}{2}$ or $\phi = \frac{3\pi}{2}$. These special cases are important in describing polarimetric states and their use will become clear in later sections.

1. In eq. 2.7 and eq. 2.8, when E_{oy} is zero, E_y is also zero leaving only the E_x component. The resulting vectorial description describes a horizontally polarised wave. Similarly, if E_{ox} is zero, this describes a vertically polarised wave.

2. With a phase delay difference of 0 or π, the polarisation ellipse in eq. 2.9 reduces to

$$\begin{aligned} \frac{E_x^2}{E_{ox}^2} + \frac{E_y^2}{E_{oy}^2} \pm 2\frac{E_x}{E_{ox}}\frac{E_y}{E_{oy}} &= 0 \\ \left(\frac{E_x}{E_{ox}} \pm \frac{E_y}{E_{oy}}\right) &= 0 \end{aligned} \tag{2.10}$$

   which has a solution of

$$E_x = \pm\left(\frac{E_{ox}}{E_{oy}}\right)E_y \tag{2.11}$$

   The solution in eq. 2.11 shows that there is a linear relation between the orthogonal components. This describes a linearly polarised wave. In the case where $\phi = 0$, there is a negative linear relation and conversely when $\phi = \pi$, the linear relation is positive. If the maximum amplitudes are equal, i.e., $E_{ox} = E_{oy}$, then this describes a $\pm 45°$ linearly polarised wave.

3. For the third case, when there is a phase delay difference of $\phi = \frac{\pi}{2}$ or $\frac{3\pi}{2}$, the polarisation ellipse reduces to being the general description of the non-rotated ellipse in eq. 2.12. In this case, unlike case two, it is not apparent whether the phase delay difference is $\phi = \frac{\pi}{2}$ or $\frac{3\pi}{2}$.

$$\frac{E_x^2}{E_{ox}^2} + \frac{E_y^2}{E_{oy}^2} = 1 \tag{2.12}$$

4. In the final case, when the maximum amplitudes are the same and the phase delay differences are the same as case three, the polarisation ellipse and eq. 2.12 reduces to

$$E_x^2 + E_y^2 = E_o^2 \tag{2.13}$$

   Depending on the phase delay difference, the resulting waves can be either right-handed circularly polarised (RHCP) or left-handed circularly polarised (LHCP). When $\phi = \frac{\pi}{2}$, the wave is RHCP and when $\phi = \frac{3\pi}{2}$, the wave is LHCP. The polarisations are named as such because if an observer places their thumb in the direction of $\mathbf{k}$, the light wave will travel radially around their thumb. If the wave travels in the direction of the fingers on their right hand, then the wave is right-hand circularly polarised and conversely named if the wave follows the fingers on their left hand. Unfortunately, again, like in case three, from the equation alone, the phase difference is ambiguous. In all the special cases, the phase difference is only clear in case two.

In this section, polarisation was formulated mathematically along with the resulting polarisation ellipse. This ellipse will degenerate to some special cases under certain circumstances and these cases will be used in later sections of this thesis for describing polarising elements and in the design of the polarimetry system.

The polarisation ellipse described here has some limitations. This ellipse will be traced out during such a short duration that it cannot be easily observed thereby making the polarisation of the light wave difficult to determine. In addition, this method assumes the light waves are entirely polarised, which could not be the case.

2.1.2 Stokes Parameters

What was mentioned in the last section motivates the search for a formulation of the polarisation ellipse in terms of observables. This was a task taken on by Gabriel Stokes in 1852 [19].

To formulate the polarisation in terms of observables, both of the orthogonal waves in eq. 2.5 and 2.6 can be imagined to be at the spatial position $z = 0$, leaving only time as the wave propagator.

$$E_x(t) = E_{ox}\cos(\omega t + \phi_x) \tag{2.14}$$

$$E_y(t) = E_{oy}\cos(\omega t + \phi_y) \tag{2.15}$$

This leads to eq. 2.9, but now with only a time dependence.

$$\frac{E_x^2(t)}{E_{ox}^2} + \frac{E_y^2(t)}{E_{oy}^2} - 2\frac{E_x(t)}{E_{ox}}\frac{E_y(t)}{E_{oy}}\cos\phi = \sin^2\phi \tag{2.16}$$

To make this observable, the time average ($\langle\cdots\rangle$) of the instantaneous amplitude term can be taken.

$$\frac{\langle E_x^2(t)\rangle}{E_{ox}^2} + \frac{\langle E_y^2(t)\rangle}{E_{oy}^2} - 2\frac{\langle E_x(t)}{E_{ox}}\frac{E_y(t)\rangle}{E_{oy}}\cos\phi = \sin^2\phi \tag{2.17}$$

where the time average is

$$\langle E_i(t)E_j(t)\rangle = \lim_{T\to\infty}\frac{1}{T}\int_0^T E_i(t)E_j(t)dt \tag{2.18}$$

Each time average is evaluated, using eq. 2.14 and 2.15 in eq. 2.18. Due to the periodicity of the monochromatic radiation, only the average over a single oscillation needs to be taken

$$\langle E_x^2(t)\rangle = \frac{1}{2}E_{ox}^2 \tag{2.19}$$

$$\langle E_y^2(t)\rangle = \frac{1}{2}E_{ox}^2 \tag{2.20}$$

$$\langle E_x(t)E_y(t)\rangle = \frac{1}{2}E_{ox}E_{oy}\cos\phi \tag{2.21}$$

and to make the waves observable, eq. 2.17 is multiplied by by $4E_{ox}^2E_{oy}^2$ and $E_{ox}^2 + E_{oy}^2$ is added to both sides of the equation to produce

$$\left(E_{ox}^2 + E_{oy}^2\right)^2 - \left(E_{ox}^2 - E_{oy}^2\right)^2 - \left(2E_{ox}^2E_{oy}^2\cos\phi\right)^2 = \left(2E_{ox}^2E_{oy}^2\sin\phi\right)^2 \tag{2.22}$$

Each of the square terms is recognized as the Stokes parameters of the light wave. The parameters are all observable intensities.

$$S_0 = E_{ox}^2 + E_{oy}^2 \tag{2.23}$$

$$S_1 = E_{ox}^2 - E_{oy}^2 \tag{2.24}$$

$$S_2 = 2E_{ox}E_{oy}\cos\phi \tag{2.25}$$

$$S_3 = 2E_{ox}E_{oy}\sin\phi \tag{2.26}$$

And if the derivation is done using the phasor representation,

$$E_x = E_{ox}e^{i\omega t}e^{i\phi_x} \tag{2.27}$$

$$E_y = E_{oy}e^{i\omega t}e^{i\phi_y} \tag{2.28}$$

the Stokes parameters take the form of

$$S_0 = E_xE_x^* + E_yE_y^* \tag{2.29}$$

$$S_1 = E_xE_x^* - E_yE_y^* \tag{2.30}$$

$$S_2 = E_xE_y^* + E_yE_x^* \tag{2.31}$$

$$S_3 = i(E_xE_y^* - E_yE_x^*) \tag{2.32}$$

Eq. 2.23, eq. 2.29 and the first term in eq. 2.22 are recognized as the full intensity of the light wave. Rearranging eq. 2.22 shows that the squared sum of S_{1-3} is equal to the square of the full intensity of the light wave, S_0, shown in eq 2.33.

$$S_0^2 = S_1^2 + S_2^2 + S_3^2 \tag{2.33}$$

The sum in eq 2.33 is true under the assumption that the wave is perfectly polarised. In the case of partial polarisation, it can be shown in eq. 2.34 that the relation in eq. 2.34 holds.

$$S_0^2 \geq S_1^2 + S_2^2 + S_3^2 \tag{2.34}$$

A metric can then be defined to describe the degree of polarisation, P, using eq. 2.33 and eq. 2.34

$$P = \frac{I_{pol}}{I_{tot}} = \frac{(S_1^2 + S_2^2 + S_3^2)^{\frac{1}{2}}}{S_0} \qquad 0 \leq P \leq 1 \tag{2.35}$$

2.1.3 Stokes Vectors

The four Stokes parameters can be expressed in terms of a vector with each element being a Stokes parameter. The use of a vector representation allows other mathematical tools to be used later on.

$$\mathbf{S} = \begin{pmatrix} S_0 \\ S_1 \\ S_2 \\ S_3 \end{pmatrix} = \begin{pmatrix} E_{ox}^2 + E_{oy}^2 \\ E_{ox}^2 - E_{oy}^2 \\ 2E_{ox}E_{oy}\cos\phi \\ 2E_{ox}E_{oy}\sin\phi \end{pmatrix} \tag{2.36}$$

Each of the special (degenerate) cases of the polarisation ellipse can be represented using this observable representation from eq. 2.36. Each representation is scaled by the intensity of the light wave, I_0.

Horizontally Polarised Light

In horizontally polarised light, $E_{oy} = 0$, eq. 2.36 reduces to

$$\mathbf{S} = I_0 \begin{pmatrix} 1 \\ 1 \\ 0 \\ 0 \end{pmatrix} \tag{2.37}$$

where $I_0 = E_{ox}^2$.

Vertically Polarised Light

In vertically polarised light, $E_{ox} = 0$, eq. 2.36 reduces to

$$\mathbf{S} = I_0 \begin{pmatrix} 1 \\ -1 \\ 0 \\ 0 \end{pmatrix} \tag{2.38}$$

where $I_0 = E_{oy}^2$.

$+45°$ Polarised Light

In $+45°$ polarised light, $E_{oy} = E_{ox} = E_o$ and $\phi = 0$, so eq. 2.36 reduces to

$$\mathbf{S} = I_0 \begin{pmatrix} 1 \\ 0 \\ 1 \\ 0 \end{pmatrix} \tag{2.39}$$

where $I_0 = 2E_o^2$

$-45°$ Polarised Light

In $-45°$ polarised light, $E_{oy} = E_{ox} = E_o$ and $\phi = \pi$, so eq. 2.36 reduces to

$$\mathbf{S} = I_0 \begin{pmatrix} 1 \\ 0 \\ -1 \\ 0 \end{pmatrix} \tag{2.40}$$

where $I_0 = 2E_o^2$.

Right-hand Circularly Polarised Light

In RHCP light, $E_{oy} = E_{ox} = E_o$ and $\phi = \frac{\pi}{2}$, so eq. 2.36 reduces to

$$\mathbf{S} = I_0 \begin{pmatrix} 1 \\ 0 \\ 0 \\ 1 \end{pmatrix} \tag{2.41}$$

where $I_0 = 2E_o^2$.

Left-hand Circularly Polarised Light

In LHCP light, $E_{oy} = E_{ox} = E_o$ and $\phi = \frac{3\pi}{2}$, so eq. 2.36 reduces to

$$\mathbf{S} = I_0 \begin{pmatrix} 1 \\ 0 \\ 0 \\ -1 \end{pmatrix} \tag{2.42}$$

where $I_0 = 2E_o^2$.

2.1.4 Mueller Matrices

Polarimetry is the measurement of how the polarisation state of light changes as it interacts with matter. The mathematical characterisation of this matter and how it changes a wave's polarisation is described using Mueller matrices.

Mueller matrices are four-by-four matrices that map an incoming light beam's Stokes representation to an outgoing light beam's Stokes representation, demonstrated in eq. 2.43, mimicking the interaction of the polarized light wave with matter: i) as it changes the amplitudes of components of the light wave, ii) as the phases change between the orthogonal components, iii) as it changes the direction of the orthogonal field components, and iv) as energy transfers from polarised to unpolarised states. This tool offers the ability, under certain constraints, to theoretically observe the change in light polarisation for a wide range of possible input Stokes vectors.

$$\mathbf{S_{out}} = \mathbf{M}\mathbf{S_{in}} \tag{2.43}$$

$$\begin{pmatrix} S_0' \\ S_1' \\ S_2' \\ S_3' \end{pmatrix} = \begin{pmatrix} m_{11} & m_{12} & m_{13} & m_{14} \\ m_{21} & m_{22} & m_{23} & m_{24} \\ m_{31} & m_{32} & m_{33} & m_{34} \\ m_{41} & m_{42} & m_{43} & m_{44} \end{pmatrix} \begin{pmatrix} S_0 \\ S_1 \\ S_2 \\ S_3 \end{pmatrix} \tag{2.44}$$

The size of the Mueller matrix requires there to be 16 measurements taken with different input and output Stokes vectors to determine the affect of matter on the polarisation of a light wave. There is no guarantee that it will result in a well posed system [21].

2.1.5 Polarising Elements

For optical experiments and polarimetry, manipulating the polarisation of the incoming and outgoing light beams is important to ensure proper light interaction [22], measurement and interaction with matter. To perform this manipulation, elements can be placed in the light path with varying effect.

Elements that are capable of changing the amplitudes of orthogonal components unequally are called polarisers or diattentuators. Elements that incur a phase change between the orthogonal components are called retarders and elements that rotate the orthogonal

components of the beam through some angle are called rotators. Each of these elements can be described using a Mueller matrix.

Polarisers

The effect the polariser on the component amplitudes of the light wave can be described using these two terminal equations

$$E'_x = p_x E_x \qquad 0 \leq p_x \leq 1 \tag{2.45}$$

$$E'_y = p_y E_y \qquad 0 \leq p_y \leq 1 \tag{2.46}$$

These representations are used as a starting point to describe the polariser's Mueller matrix. Substituting eq. 2.45 and 2.46 into eq. 2.23–2.26 produces a new Stokes vector, S', as the output of the polariser.

$$S'_0 = p_x^2 E_{ox}^2 + p_y^2 E_{oy}^2 \tag{2.47}$$

$$S'_1 = p_x^2 E_{ox}^2 - p_y^2 E_{oy}^2 \tag{2.48}$$

$$S'_2 = 2 p_x p_y E_{ox} E_{oy} \cos\phi \tag{2.49}$$

$$S'_3 = 2 p_x p_y E_{ox} E_{oy} \sin\phi \tag{2.50}$$

This can be reformulated into the form of eq. 2.43 as

$$\begin{pmatrix} S'_0 \\ S'_1 \\ S'_2 \\ S'_3 \end{pmatrix} = \frac{1}{2} \begin{pmatrix} p_x^2 + p_y^2 & p_x^2 - p_y^2 & 0 & 0 \\ p_x^2 - p_y^2 & p_x^2 + p_y^2 & 0 & 0 \\ 0 & 0 & 2p_x p_y & 0 \\ 0 & 0 & 0 & 2p_x p_y \end{pmatrix} \begin{pmatrix} S_0 \\ S_1 \\ S_2 \\ S_3 \end{pmatrix} \tag{2.51}$$

In the case of a perfectly ideal horizontal polariser (i.e., $p_x = 1$, $p_y = 0$), the above Mueller matrix becomes

$$\mathbf{M_H} = \frac{1}{2} \begin{pmatrix} 1 & 1 & 0 & 0 \\ 1 & 1 & 0 & 0 \\ 0 & 0 & 0 & 0 \\ 0 & 0 & 0 & 0 \end{pmatrix} \tag{2.52}$$

And conversely, if it was a perfectly ideal vertical polariser (i.e., $p_x = 0$, $p_y = 1$), then the Mueller matrix becomes

$$\mathbf{M_V} = \frac{1}{2}\begin{pmatrix} 1 & -1 & 0 & 0 \\ -1 & 1 & 0 & 0 \\ 0 & 0 & 0 & 0 \\ 0 & 0 & 0 & 0 \end{pmatrix} \tag{2.53}$$

In the case of commercially available polarisers, such as wire grid, stretched polymer, glass, or nanoparticle polarisers, they are never perfectly polarising (i.e., $p_x p_y \neq 0$). Therefore, the term $2p_x p_y$ does not go to zero and the polariser does not create perfectly linearly polarised light, but instead elliptically polarised light. To describe the lack of ideal performance, a metric called extinction ratio is used by manufacturers and defined in eq. 2.54.

$$e = \frac{p_p}{p_s} \tag{2.54}$$

where p_p is the larger scaling factor in the direction parallel to the polarising direction and p_s is the scaling factor in the cross (perpendicular) direction to the polarising. It can be seen that in the case of a horizontal polariser, $p_p = p_x$ and $p_s = p_y$ and conversely in the case of a vertical polariser, $p_p = p_y$ and $p_s = p_x$. Typically the extinction ratio is in the range of $10^4 - 10^7$.

Retarders

Retarding elements produce a phase delay difference between the orthogonal components of a light wave. From the derivation of the polarisation ellipse and its' special (degenerate) cases, the application of a retarder is needed to produce these cases. The effect of the retarder can be described using the two terminal equations

$$E'_x = e^{+i\delta/2} E_x \tag{2.55}$$

$$E'_y = e^{-i\delta/2} E_y \tag{2.56}$$

where δ is the incurred retardation by the retarding element. For mathematical convenience, the retardation will be split between the two orthogonal components, $-\delta/2$ for E_y and $+\delta/2$ for E_x. Taking the above representations into eq. 2.29–2.32, the resulting Stokes parameters are

$$S'_0 = S_0 \tag{2.57}$$

$$S_1' = S_1 \tag{2.58}$$

$$S_2' = S_2 \cos\delta + S_3 \sin\delta \tag{2.59}$$

$$S_3' = -S_2 \sin\delta + S_3 \cos\delta \tag{2.60}$$

The Mueller matrix to create the Stokes parameters above is shown in eq. 2.61.

$$\mathbf{M}_\delta = \begin{pmatrix} 1 & 0 & 0 & 0 \\ 0 & 1 & 0 & 0 \\ 0 & 0 & \cos\delta & \sin\delta \\ 0 & 0 & -\sin\delta & \cos\delta \end{pmatrix} \tag{2.61}$$

Rotators

There are elements in the lab, and in nature (such as sugars and amino acids [19]), that can cause a rotation in polarised light and these elements can also be characterised using Mueller matrices. To derive these Mueller matrices, a paradigm is necessary to describe the rotation. This is described in Figure 2.1. In this figure, there is some wave, E, linearly polarised at an angle β from the horizontal, in x, y, and it is rotated by θ. Both angles are defined counter-clockwise from the horizontal. Two sets of terminal equations are used here. The first set refer to the polarisation of the wave relative to the rotated coordinated system, x', y', and the second set refers to the original coordinate system, x, y. In the x', y' coordinate space

$$E_x' = E\cos(\beta - \theta) \tag{2.62}$$

$$E_y' = E\sin(\beta - \theta) \tag{2.63}$$

and in the original x, y coordinate space

$$E_x = E\cos\beta \tag{2.64}$$

$$E_y = E\sin\beta \tag{2.65}$$

Expanding the first set and using the second set

$$E_x' = E_x\cos\theta + E_y\sin\theta \tag{2.66}$$

$$E_y' = -E_x\sin\theta + E_y\cos\theta \tag{2.67}$$

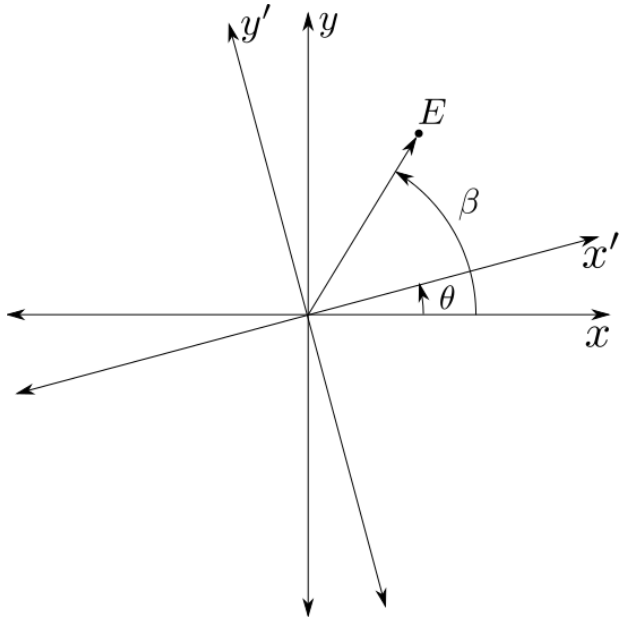

Figure 2.1: Rotated coordinate system for rotating polarising element.

results in the Stokes parameters

$$S_0' = S_0 \tag{2.68}$$

$$S_1' = S_1 \cos 2\theta + S_2 \sin 2\theta \tag{2.69}$$

$$S_2' = -S_1 \sin 2\theta + S_2 \cos 2\theta \tag{2.70}$$

$$S_3' = S_3 \tag{2.71}$$

leading to a Mueller matrix described in eq. 2.72.

$$\mathbf{M}_{rot}(2\theta) = \begin{pmatrix} 1 & 0 & 0 & 0 \\ 0 & \cos 2\theta & \sin 2\theta & 0 \\ 0 & -\sin 2\theta & \cos 2\theta & 0 \\ 0 & 0 & 0 & 1 \end{pmatrix} \tag{2.72}$$

2.1.6 Polarimetric Systems

Polarimetry typically involves five components: the source, the polarising elements (i.e., polarisers, retarders, and/or rotators), the matter, the analyser, and the detector. This

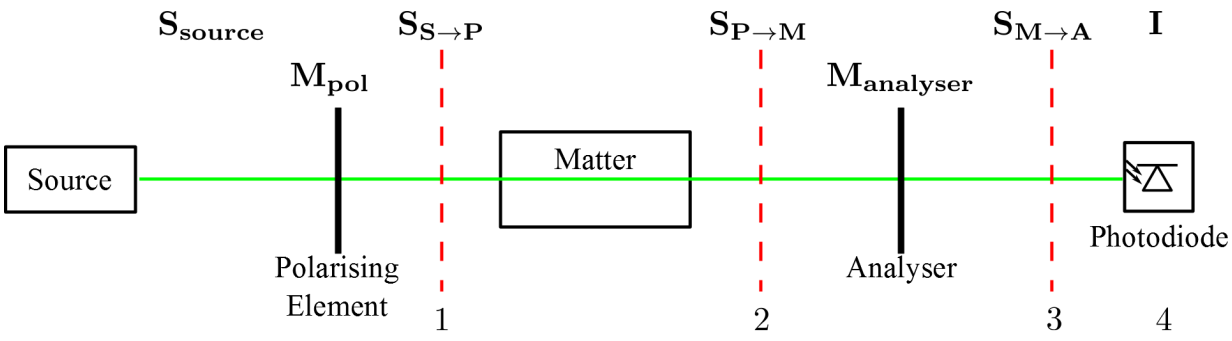

Figure 2.2: Pictorial representation of a polarimetry system.

system can be split into four parts. Each of these four parts represent a single change in the light wave's polarisation: i) source through polarising element, ii) polarising element through matter, iii) through analyser to detector, and iv) light beam flux to measured intensity in the detector. The full system and these parts are shown in Figure 2.2.

1. The outgoing intensity from the source can be modelled as a Stokes vector, $\mathbf{S_{source}}$, and some Mueller matrix can be used to represent the set of polarising elements, $\mathbf{M_{pol}}$.
$$\mathbf{S_{S\to P}} = \mathbf{M_{pol}}\mathbf{S_{source}} \tag{2.73}$$

2. Next is the change in polarisation that occurs when the incoming wave interacts with matter, $\mathbf{M_{matter}}$.
$$\mathbf{S_{P\to M}} = \mathbf{M_{matter}}\mathbf{S_{S\to P}} \tag{2.74}$$

3. The passing of the light wave through the analyser, $\mathbf{M_{analsyer}}$ is
$$\mathbf{S_{M\to A}} = \mathbf{M_{analsyer}}\mathbf{S_{P\to M}} \tag{2.75}$$

4. When the Stokes parameter are converted to the measured intensity on the detector, there will be a matrix $\mathbf{A}$. This matrix describes how the energy from the light beam will be converted into information from the detector. This makes the resulting measurements on the detector
$$\mathbf{I_D} = \mathbf{A}\mathbf{S_{M\to A}} \tag{2.76}$$
where $\mathbf{I_D}$ is a vector with a single non-zero value. This non-zero value is what the detector produces as a measurement.

Typically detectors measure the intensity of the light beam, which makes $\mathbf{A}$

$$\mathbf{A} = \begin{pmatrix} 1 & 0 & 0 & 0 \\ 0 & 0 & 0 & 0 \\ 0 & 0 & 0 & 0 \\ 0 & 0 & 0 & 0 \end{pmatrix} \tag{2.77}$$

Matrix $\mathbf{A}$ will be different depending on the kind of detector used, or the kind of polarimetry being performed. For example, if a detector that was sensitive only to horizontally polarised light is used in a polarimeter, then $\mathbf{A}$ will be

$$\mathbf{A} = \begin{pmatrix} 1 & 1 & 0 & 0 \\ 0 & 0 & 0 & 0 \\ 0 & 0 & 0 & 0 \\ 0 & 0 & 0 & 0 \end{pmatrix} \tag{2.78}$$

For this thesis, we will use eq. 2.77 as $\mathbf{A}$.

With the configuration in Figure 2.2, the polarisation analyser, i.e., $\mathbf{M_{analyser}}$, can be arranged in several ways to determine the polarisation of the light wave. There are rotating element arrangements, phase modulation arrangements and oscillating element arrangements. This thesis will use the rotating element arrangement and will elaborate in the theoretical formulation of the proposed device later in this thesis. Information on the other two arrangements can be found in Goldstein [19] and Collett [20].

Rotating Element Analyser

In the case of a rotating element analyser, the analyser can be modelled as a rotated polarising element, similar to what was outlined in Section 2.1.5.

So far, the formulations for polarising elements have been done assuming the attenuating directions are parallel to the orthogonal coordinate system x, y. In the case of a rotated polarising element, it can be assumed that there is some x', y' coordinate system where the polarising element is not rotated and our prior formulations hold. With the assumption that the coordinate system is on-axis with the light beam, there can be an angle, θ, that describes the angular displacement of x', y' from x, y. The coordinate systems are shown in Figure 2.3. With the assumptions used in the derivation of the light wave and the polarising elements, the wave must be described in a coordinate system that is parallel

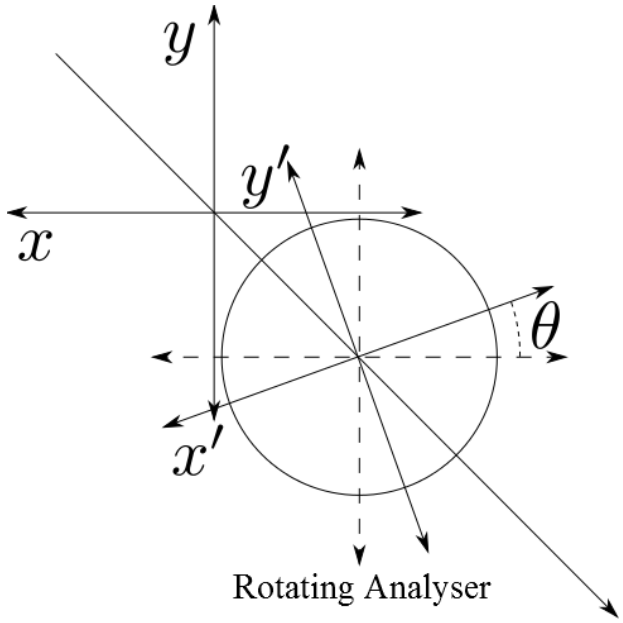

Figure 2.3: Graphical representation of the coordinate systems to mathematically formulate the Mueller matrix for an element rotated by θ.

to the directions of the polarising element for interaction to occur. After interaction, the light wave needs to again be described in the original coordinate system for any subsequent interaction. All this can be described using the formulation below

$$\mathbf{M_{analsyer}} = \mathbf{M}_{rot}(-2\theta)\mathbf{M}\mathbf{M}_{rot}(2\theta) \tag{2.79}$$

where $\mathbf{M}$ is the Mueller matrix of some polarising element and $\mathbf{M}_{rot}$ is the Mueller matrix defined in eq. 2.72.

Ultimately, the system can be formulated from source to detector as eq. 2.80.

$$\mathbf{I} = \mathbf{A}\mathbf{M}_{rot}(-2\theta)\mathbf{M}\mathbf{M}_{rot}(2\theta)\mathbf{M_{matter}}\mathbf{M_{pol}}\mathbf{S_{source}} \tag{2.80}$$

The $\mathbf{A}$ matrix used to convert the observables to intensities can be perturbed from its' non-ideal state to include intensity modulations and variations spatially and temporally. The next two sections in this chapter will describe the variations that can occur and methods for their reduction thereby enhancing the polarimetric measurements.

2.2 System Polarimetric Measurement Enhancement

Intensity variations in polarimetric measurements can occur from imperfections in the polarising elements, from their arrangement relative to one another, and from detector characteristics.

From a system design perspective, one can perform measurement enhancement by ensuring that elements are chosen and placed in such a way that any possible variance in the measurements are reduced. Vaughn *et al.* and Tyo approached this problem by minimizing the condition number of the overall Mueller matrix of the optical elements in the system [23, 24]. Le Juene *et al.* take another approach by minimizing the χ^2 function of the noise variance [25]. These methods are capable of increasing the signal-to-noise ratio by several tens of decibels through the optimal choice of polarising element placement.

Tyo's work is of particular interest to this thesis for his use of spatial simulation data to mimic the temporal polarimetric measurements for each of the Stokes vectors. This will be discussed more in Section 2.3.

Intensity variations seen by the detector are not explicitly addressed in the system design of polarimeters and cannot easily be suppressed. The reason being that the variations are either inherent from the physics of the light beam being measured, i.e., speckle and

shot noise, or from the electronics, i.e., dark current noise, read-out noise and fixed pattern noise. Typically, any enhancement on the detector is handled through post processing methods or ignored [23].

2.3 Computational Polarimetric Measurement Enhancement

The intensity projected on the photosensitive areas of a detector can not only be subject to modulations from the arrangement of polarising elements, but also from additional intensity variations from inherent physical or detector characteristics.

There are two kinds of intensity variations that can be introduced at the detector: i) intensity variations from the inherent characteristics of the measured light, and ii) intensity variations from the inherent characteristics of the electronics involved. From here on, this thesis will make a distinction between these kinds of intensity variations: error and noise. Error is a deterministic quantity that is constant through time, while noise is a stochastic value that is temporally varying.

2.3.1 Physical Intensity Variations

Lasers are useful sources in polarimetry due to their monochromatic nature. Matter can have varying polarimetric responses across the spectrum making it difficult to model using Mueller matrices, given the assumptions stated in their formulation (see Section 2.1). Lasers are also coherent sources (i.e., the phase difference between two temporal or spatial points in the wave emitted is constant) which results in speckle. Speckle is a kind of error that causes variation in the spatial intensity distribution due to the interference of coherent wavefronts. This spatial pattern differs depending on the material scattered and wavelength used, but is constant through time.

As found in Vaughn *et al.*, speckle is a consequence that can be experienced in polarimetry [23], but in polarimetric applications for matter analysis that use the full laser spot, methods for speckle removal have been explored in so far as the methods explained in Section 2.2. Computational methods for polarimetric speckle reduction in matter identification have not been explored, as far as this author knows.

Another fundamental noise source on the detector is the statistical arrival of incident photons. This is called shot noise and is typically modelled as a Poisson process. This is

a temporally varying noise source, but as more and more photons become integrated on the detector, the intensity variations can be modelled more as a Gaussian process. This is explained further in Chapter 4.

Shot noise is considered in the works of Vaughn *et al.* and Le Jeune *et al.*. They recognize shot noise as a cause of variance in the measurements for matter identification polarimetry, but pay no special attention to its' Poisson characteristics [23, 25].

2.3.2 Electrical Intensity Variations

Detectors are transducers that use photosensitive areas and convert them to electrical signals that can later be interpreted. In the transducer itself, there are electrical processes that are necessary and common amongst most detectors that can cause temporal intensity variations. These variations are modelled as zero-mean Gaussian distributions.

For an ideal intensity perturbed by zero-mean Gaussian noise, the observed intensity can be modelled as:

$$\mathcal{U} = \mathcal{I} + \eta \tag{2.81}$$

where $\mathcal{U}$ is the observed intensity, $\mathcal{I}$ is the ideal intensity and η is a value sampled from a zero-mean Gaussian noise process ($\eta \sim \mathcal{N}(0, \sigma^2)$). The most common method to address Gaussian noise is to observe the intensity N times

$$\hat{\mathcal{U}} = \frac{1}{N} \sum_{i=0}^{N} (\mathcal{I}_i + \eta_i) \tag{2.82}$$

where $\hat{\mathcal{U}}$ is the enhanced signal such that $\hat{\mathcal{U}} \sim \mathcal{I}$. As N approaches a large number, the average of η will approach zero, since it is sampled from a zero-mean Gaussian distribution, leaving the observed intensity equal to the real intensity. One method is to capture N observations is through time, but this is difficult to do when measuring dynamic phenomena. Polarimetry is typically used in static scenarios and these observations can be captured with no issue [17]. However, from a usability perspective, being able to capture N observations can take a noticeable amount of time.

Tyo had performed an interesting simulation in his work in polarimetric enhancement where he uses a two-dimensional representation to simulate the temporal arrival of measurements from a photosensitive area [24]. In other words, he equates the spatial multiplexing

in the two-dimensional image to the temporal multiplexing that occurs on a photosensitive area. This is used as inspiration for two main contributions of this thesis.

2.4 Summary

This chapter summarised the theoretical tools used in describing the polarisation state of a light beam and the methods for analysing its' interaction with polarising elements and matter. Unfortunately, these polarising elements are not perfect in their polarising effects which causes undesirable polarisation states, as alluded to in Section 2.1.5. Analysis of these imperfections and their affect on the polarimetric measurements is done in Chapter 3.

This chapter also summarised prior work in measurement enhancement methods to reduce the effect of intensity variations on polarimetric measurements. Most of the prior work is primarily concentrated on polarising element arrangements to reduce quantitative metrics of Mueller matrices with the aim to reduce any intensity variation from poor arrangement. There are sources of intensity variation, such as noise, that cannot be reduced this way. Prior work on reducing the variations from these noise sources is limited to using many temporal acquisitions and averaging. This thesis will formulate and implement other methods for measurement enhancement utilising a spatial detector array in Chapters 4– 6.

Chapter 3

System Design

The current market of polarimeters for determining the concentration of chiral molecules in a solution is populated with tabletop devices with large footprints that use complex optical systems to accurately measure the complete polarisation state. The cost of this accuracy and complexity is high, with one such machine, the Thorlabs PAX5720 polarimeter, costing 8000 USD. These two reasons have constrained polarimetry to be an exclusive lab-only mode of measurement. As one of the main contributions of this thesis, we propose, design and build an inexpensive, compact polarimeter that can be used outside the lab. This chapter will outline the design of the polarimeter.

We will start with an explanation and justification for the governing theoretical principles behind the design of the polarimeter, then propose a contraption to arrange the parts of the polarimeter. And finally, we will theoretically analyse the system, using the tools and methods mentioned in Section 2.1, taking into account non-ideal characteristics; introducing imperfect polarisers and retarders.

3.1 Polarimetric Principle

The polarimeter use two principles to guide its' development and analysis: i) amplitude division, and ii) perfect polarisation.

3.1.1 Amplitude Division

This polarimeter uses amplitude division rather than wavefront division for polarimetry. The reasons for this choice were to avoid the imperfections and inconsistencies that can arise from the use of wavefront division devices:

1. The most common method for wavefront division polarimetry are micropolarisers. Micropolariser arrangements are arrays of nanofabricated apertures that are capable of polarising light waves. These apertures can be in the form of actual holes or grids of metal wire [19].

   The sizes of the micropolariser apertures are on the order of several wavelengths. This is well within the size for diffraction to have non-trivial effects. Diffraction causes pixel cross-talk to occur between the different micropolarisers, thereby producing spatial intensity variations and contamination of the measurements [12].

2. Micropolariser polarimetry is a young field of study and fabricating a polarising element array is expensive. It is very common for there to be some uncertainty in the measurements due to imperfections in manufacturing of the array in a size necessary for chiral molecule identification.

3. Micropolarisers perform quite well under conditions where the incident wavefront is planar. This assumption doesn't hold in applications requiring polarimetry for matter identification since matter does not typically allow light to maintain spatial coherence [12].

With the use of amplitude division methods, we can avoid all the issues outlined above. The tradeoff, however, is that amplitude division splits the total energy of the wave, thereby decreasing the intensity of the incident wave at every subsequent measurement.

3.1.2 Perfect Polarisation

Another principle used in this design is that eq. 2.33 holds. This implies that any material being analysed in this system is perfectly polarising with $P = 1$, from eq. 2.33. The implication is that only four measurements need be taken, rather than seven [2]. However, the modular design outlined in Section 3.2, allows for the elements to be interchanged to accommodate materials where $P < 1$, from eq. 2.34.

3.2 System Design

This section will outline the design of the inexpensive, compact polarimeter for measuring chiral molecule concentration. The device will be described in the following order: i) illumination source and amplitude division, ii) cuvette analyser, and iii) detector.

3.2.1 Illumination and Amplitude Division

To minimize the cost of the device, an easy way to start is to reduce the amount of illumination sources used. Hence, this design will use a single source and undergo amplitude division to imitate four sources. There are several ways to perform this division, such as using prisms and crystals. To meet the requirement for minimizing cost and size, arrangement of beam splitters will be used with a single laser.

The beamsplitters are arranged in a three-by-one column punctuated with a mirror. This configuration is demonstrated in Figure 3.1. Four beams are produced that can then be transmitted into the next component of this polarimeter: the cuvette analyser.

3.2.2 Cuvette Analyser

The three reflected beams from the beamsplitters and the one reflected from the mirror produce four independent beams that can be manipulated for the purpose of analysing the solution.an array of polarising elements can be placed in the path of each beam to achieve a particular known polarisation before interacting with the solution. Similarly, upon exit of the solution, it can be assumed that the beams have not scattered enough to interfere with another, so another array of polarising elements can be introduced in the path of the beams to analyse their polarisation change. The four polarising and analysing elements are secured in a filter holder, shown in Figure 3.2.

To perform this analysis, a single body element was designed to secure the polarising elements, cuvette of solution, and analysing elements and have them maintain a constant orientation with one another. This is to reduce any intensity loss that could occur from misalignment and refraction. This element and the placement of the polarising elements, cuvette of solution, and analysing elements is shown in Figure 3.3.

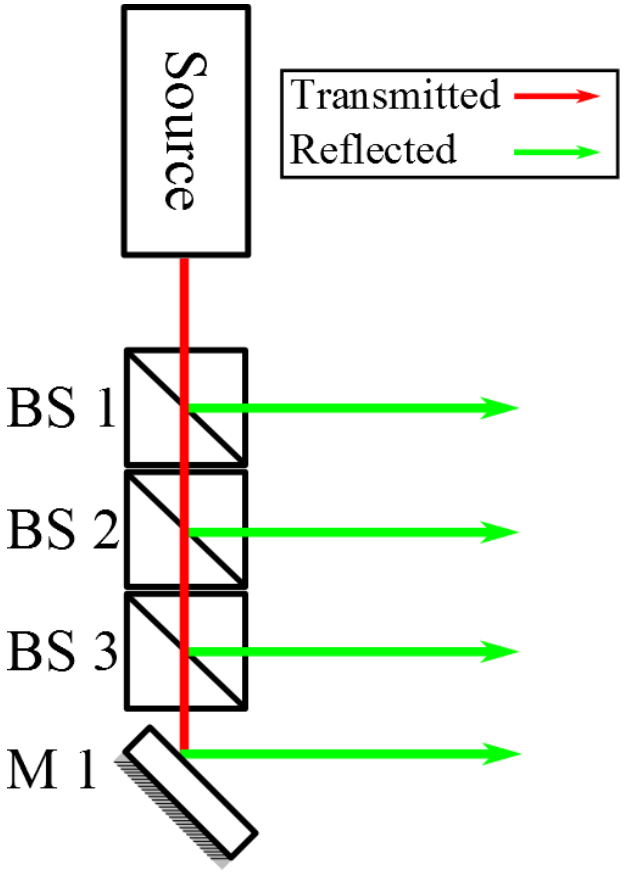

Figure 3.1: Configuration of beamsplitters (BS) and mirrors (M) as a compact illumination design for amplitude division.

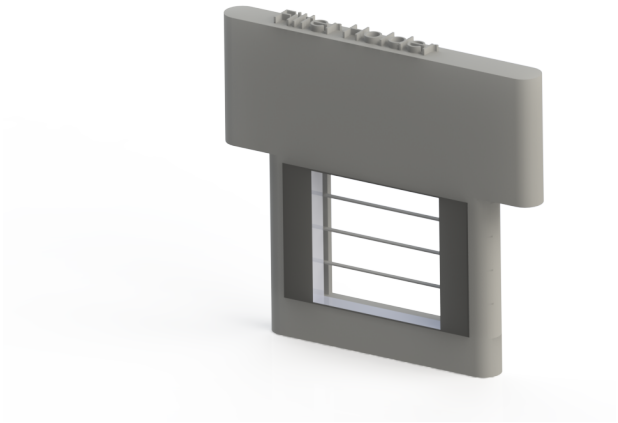

Figure 3.2: Holder for the polarisation and analyser filter arrays.

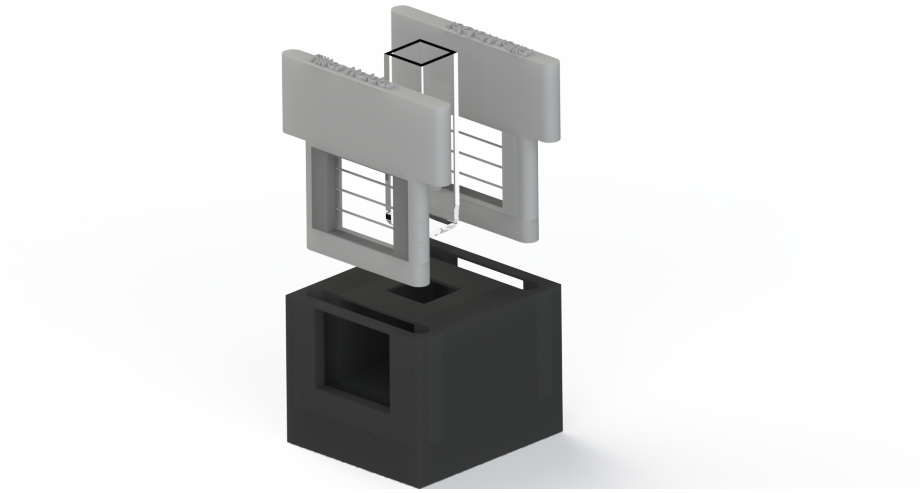

Figure 3.3: Holder to maintain parallel orientation of filters with cuvette of solution.

3.2.3 Detector

The four light beams will be incident on the detector after they pass through the analysing elements. The output from the detector is the integration of the wave amplitude over a duration of time; however, there are imperfections in the conversion of the wave energy into pixel value, which we will explore and compensate for later.

Detectors output a digital signal with a limited number of bits per pixel. These bits represent the intensity of the pixel quantised within a range from the lowest pixel value, or zero, to the highest. This poses a unique problem for this system because of the beam-splitter arrangement from the light source. The wave energy will be decreasing, from the first beam to the last, thereby increasing the range of the intensities on the detector. This causes the system to lose accuracy due to an error known as quantisation error.

To increase the detector pixel accuracy, the wave amplitudes need to be kept to roughly the same amount. To this end, neutral density (ND) filters are used after the beamsplitters to attain a similar wave amplitude from all the reflected beams. This configuration is shown in Figure 3.4.

The overall system, with the components described in the sections above, is rendered in Figure 3.5. In Section 3.3, the system is modelled with tools from Section 2.1 to find the Stokes parameters.

3.2.4 System Cost and Size

The system proposed and designed in this thesis is built at a low-cost relative to the purchasing price of a tabletop, lab polarimeter. Table 3.1 lists the parts used in building this system and also their prices. With a total price of 2570.00 USD, this polarimeter costs 68% less than the Thorlabs PAX5720.

[1] https://www.thorlabs.com/thorproduct.cfm?partnumber=CPS182

[2] https://www.thorlabs.com/thorproduct.cfm?partnumber=BS007

[3] https://www.thorlabs.com/thorproduct.cfm?partnumber=NE03B

[4] http://www.thorlabs.com/thorproduct.cfm?partnumber=PF03-03-P01

[5] http://www.edmundoptics.com/optics/polarizers/linear-polarizers/high-contrast-linear-polarizing-film/86186/

[6] http://www.edmundoptics.com/optics/polarizers/waveplates-retarders/polymer-waveplates-retarders/90941/

[7] http://www.edmundoptics.com/cameras/usb-cameras/point-grey-grasshopper-3-high-performance-usb-3-0-88607/

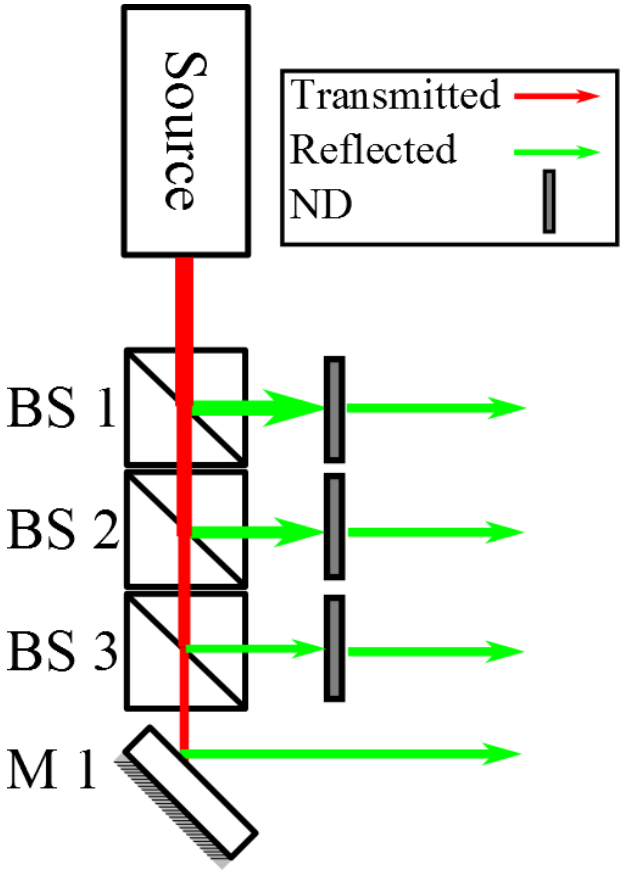

Figure 3.4: Beamsplitter (BS), mirror (M), and neutral density (ND) filter arrangement to attain a constrained amplitude range incident upon detector.

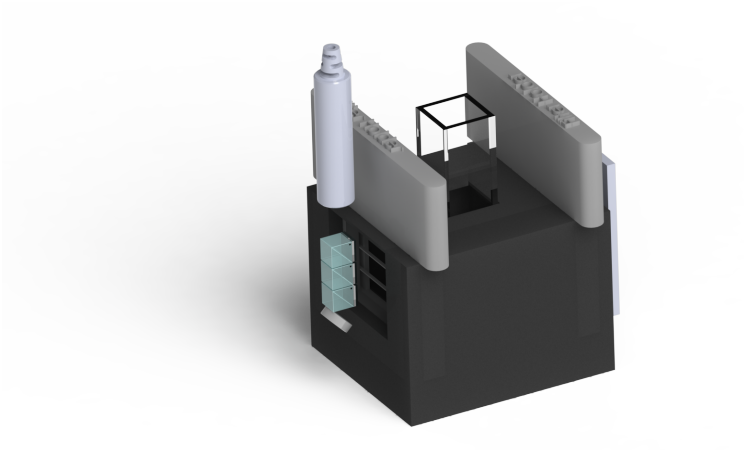

Figure 3.5: Rendering of the full polarimetric imaging system.

Table 3.1: Cost of parts for the compact polarimetry system.

Part	Unit Price (USD)	Quantity	Extended Price (USD)
5 mW Laser Diode (Thorlabs, NJ) [1]	82.00	1	82.00
50:50 Non-polarising Beamsplitter (Thorlabs, NJ) [2]	147.00	3	441.00
Absorptive ND Filter, OD: 0.3 (Thorlabs, NJ) [3]	32.00	3	96.00
Protected Silver Mirror (Thorlabs, NJ) [4]	26.00	1	26.00
High Contrast Linear Polariser (Edmund Optics, NJ) [5]	22.50	8	180.00
$\lambda/4$ Retarder (Edmund Optics, NJ) [6]	395.00	1	395.00
GS3-U3-23S6M-C Camera (Point Grey, Canada) [7]	1,350.00	1	1,350.00
		Total Price	2570.00

With this set of optical elements and light source in the arrangement described in this chapter, the polarimeter is roughly $6.5 \times 4.4 \times 7.3$ cm in size.

3.3 System Analysis

The system designed in the prior section can be analysed using Mueller matrices. The perfectly polarising principle is used, thereby making the only necessary analysing elements:

1. Horizontal polariser
2. Vertical polariser
3. $+45°$ polariser
4. Right-hand circular polariser

All four of these elements require the use a linear polariser, with one requiring an additional $\pi/2$ or quarter-wave retarder. As mentioned in Section 2.1, commercial-grade polarisers are not perfectly diattenuating in either the horizontal or vertical direction, i.e., $p_y p_x \neq 0$. This requires manufacturers of polarisers to provide an extinction ratio for their polarisers. The Mueller matrix for a general linear polariser is

$$\frac{1}{2}\begin{pmatrix} p_x^2 + p_y^2 & p_x^2 - p_y^2 & 0 & 0 \\ p_x^2 - p_y^2 & p_x^2 + p_y^2 & 0 & 0 \\ 0 & 0 & 2p_x p_y & 0 \\ 0 & 0 & 0 & 2p_x p_y \end{pmatrix} \tag{3.1}$$

Each beam in the system starts from the illumination source and then undergoes a power correction before it enters the initial polarising elements. The beamsplitters have some normalised transmission coefficients b_r and b_t. They represent the percentage of light transmitted through reflection and transmission, respectively, from the beamsplitter. The input intensity of each beam into the polarising elements, $\mathbf{I_b}$, is related to the original intensity of the laser, $\mathbf{I_o}$, where $\| \mathbf{I_o} \| = I_o$, through matrix $\mathbf{B}$ for the beamsplitter coefficients and $\mathbf{D}$ for the ND filters

$$\mathbf{I_b} = \mathbf{DBI_o} \tag{3.2}$$

where

$$\mathbf{I_o} = \begin{pmatrix} 1 \\ 1 \\ 1 \\ 1 \end{pmatrix} I_o \tag{3.3}$$

$$\mathbf{I_b} = \begin{pmatrix} I_1 \\ I_2 \\ I_3 \\ I_4 \end{pmatrix} \tag{3.4}$$

$$\mathbf{B} = \begin{pmatrix} b_r & 0 & 0 & 0 \\ 0 & b_t b_r & 0 & 0 \\ 0 & 0 & b_t b_t b_r & 0 \\ 0 & 0 & 0 & b_t b_t b_t \end{pmatrix} \tag{3.5}$$

$$\mathbf{D} = \begin{pmatrix} \frac{b_t b_t b_t}{b_r} & 0 & 0 & 0 \\ 0 & \frac{b_t b_t}{b_r} & 0 & 0 \\ 0 & 0 & \frac{b_t}{b_r} & 0 \\ 0 & 0 & 0 & 1 \end{pmatrix} \tag{3.6}$$

In the system described by Figure 2.2, this makes the incoming Stokes vector into the polarising elements an unpolarised beam with intensity

$$(\mathbf{S_{source}})_i = \begin{pmatrix} 1 \\ 0 \\ 0 \\ 0 \end{pmatrix} I_i \quad \text{where } i = 1, 2, 3, 4 \tag{3.7}$$

The system uses BS007, 50-50 beamsplitters, with a 635 nm laser from Thorlabs Inc (Thorlabs, NJ). This makes $b_r \approx b_t = 0.50$, thereby making the ND coefficient matrix, $\mathbf{D}$, reduce to

$$\mathbf{D_{50\text{-}50}} = \begin{pmatrix} 0.25 & 0 & 0 & 0 \\ 0 & 0.50 & 0 & 0 \\ 0 & 0 & 1 & 0 \\ 0 & 0 & 0 & 1 \end{pmatrix} \tag{3.8}$$

implying that we do not need a neutral density filter on I_3, reducing the total cost.

The path of each beam after it leaves the beamsplitter-ND arrangement is outlined below with the appropriate Mueller matrix. This analysis follows the same form as outlined in Section 2.1.6. For the sake of simplicity, it will be assumed that the polarising elements, $\mathbf{M_{pol}}$, are ideal. The polarising elements transform the light beams into a single degenerate polarisation state each (i.e., $\mathbf{S_{S\rightarrow P}}$ is a degenerate state) and in the following system analysis, will remain ambiguous until later in this section. With this in mind, the analysis will begin at eq 2.74. For the sake of conciseness, the symbolic version of the Mueller matrices will be used in the analysis. We can define the Mueller matrix of the solution as:

$$\mathbf{M_{matter}} = \begin{pmatrix} m_{11} & m_{12} & m_{13} & m_{14} \\ m_{21} & m_{22} & m_{23} & m_{24} \\ m_{31} & m_{32} & m_{33} & m_{34} \\ m_{41} & m_{42} & m_{43} & m_{44} \end{pmatrix} \tag{3.9}$$

1. The first light beam will encounter the solution and then a horizontal analyser before it arrives at the detector. With a horizontal analyser, the extinction ratio is defined as $\frac{p_x^2}{p_y^2}$. For simplicity, the polariser matrix is redefined as

$$\mathbf{M_H} = \frac{1}{2}\begin{pmatrix} 1+e & 1-e & 0 & 0 \\ 1-e & 1+e & 0 & 0 \\ 0 & 0 & 2\sqrt{e} & 0 \\ 0 & 0 & 0 & 2\sqrt{e} \end{pmatrix} \tag{3.10}$$

   where

$$e = \frac{p_y^2}{p_x^2} \tag{3.11}$$

   This reduced matrix approaches the representation of an ideal horizontal polariser (eq. 2.52) as $e \rightarrow 0$.

   With the above matrices defined, the intensity of the light incident on the detector after going through the solution and the analyser, $\mathbf{I_D}$, can be determined.

$$\mathbf{I_D} = \mathbf{A}\mathbf{M_H}\mathbf{M_{matter}}\mathbf{S_{S\rightarrow P}} \tag{3.12}$$

2. To find the vertical polarisation of the light beam incident on the detector after it travels through the solution and a vertical analyser, the same theoretical tools

employed in the prior beam are used. The only difference now being in the analyser, the extinction ratio is $\frac{p_y^2}{p_x^2}$. In this case, we can reduce the analyser now to

$$\mathbf{M_V} = \frac{1}{2}\begin{pmatrix} e+1 & e-1 & 0 & 0 \\ e-1 & e+1 & 0 & 0 \\ 0 & 0 & 2\sqrt{e} & 0 \\ 0 & 0 & 0 & 2\sqrt{e} \end{pmatrix} \tag{3.13}$$

And again, as $e \to 0$, the Mueller matrix becomes an ideal vertical polariser (eq. 2.53).

Using this reduced analyser matrix, $\mathbf{I_D}$ becomes

$$\mathbf{I_D} = \mathbf{A}\mathbf{M_V}\mathbf{M_{matter}}\mathbf{S_{S\to P}} \tag{3.14}$$

3. To capture the $+45°$ polarisation intensity incident on a detector after it has passed through matter, the horizontal polariser is rotated by $+45°$ degrees. To analyse this, a rotating Mueller matrix is applied to the polariser.

   A common error that can occur when placing the rotated polariser is an error in the rotated angle. This error is referred to as ϵ_θ. A rotating Mueller matrix (eq. 2.72) with this error is defined as

$$\mathbf{M_{rot}}\left(2\left(\theta+\epsilon_\theta\right)\right) = \begin{pmatrix} 1 & 0 & 0 & 0 \\ 0 & \cos(2(\theta+\epsilon_\theta)) & \sin(2(\theta+\epsilon_\theta)) & 0 \\ 0 & -\sin(2(\theta+\epsilon_\theta)) & \cos(2(\theta+\epsilon_\theta)) & 0 \\ 0 & 0 & 0 & 1 \end{pmatrix} \tag{3.15}$$

   With this source of error, the analyser Mueller matrix becomes

$$\mathbf{M_{analyser}} = \mathbf{M_{rot}}\left(-2\left(\theta+\epsilon_\theta\right)\right)\mathbf{M_H}\mathbf{M_{rot}}\left(2\left(\theta+\epsilon_\theta\right)\right) \tag{3.16}$$

   thereby making the intensity incident on the detector

$$\mathbf{I_D} = \mathbf{A}\mathbf{M_{rot}}\left(-2\left(\theta+\epsilon_\theta\right)\right)\mathbf{M_H}\mathbf{M_{rot}}\left(2\left(\theta+\epsilon_\theta\right)\right)\mathbf{M_{matter}}\mathbf{S_{S\to P}} \tag{3.17}$$

4. The final beam is analysed using a RHCP filter after passing through the solution. To do this, the analyser has to be a combination of a $+45°$ polariser and a quarter-wave retarder i.e., a retarder that produces a $\frac{\pi}{2}$ phase delay difference between the orthogonal components. A new source of error here is the retardation error, ϵ_δ. This

error comes about from the phase delay difference variation that can occur due to wavelength dependence. This would modify the retardation Mueller matrix (eq. 2.61) to become

$$\mathbf{M}_{\delta}\left(\delta+\epsilon_{\delta}\right)=\begin{pmatrix}1 & 0 & 0 & 0\\ 0 & 1 & 0 & 0\\ 0 & 0 & \cos\left(\delta+\epsilon_{\delta}\right) & \sin\left(\delta+\epsilon_{\delta}\right)\\ 0 & 0 & -\sin\left(\delta+\epsilon_{\delta}\right) & \cos\left(\delta+\epsilon_{\delta}\right)\end{pmatrix} \tag{3.18}$$

The Mueller matrix for the analyser becomes

$$\mathbf{M_{analyser}}=\mathbf{M_{rot}}\left(-2\left(\theta+\epsilon_{\theta}\right)\right)\mathbf{M_{H}}\mathbf{M_{rot}}\left(2\left(\theta+\epsilon_{\theta}\right)\right)\mathbf{M}_{\delta}\left(\delta+\epsilon_{\delta}\right) \tag{3.19}$$

thereby making the intensity incident on the detector

$$\mathbf{I_{D}}=\mathbf{A}\mathbf{M_{rot}}\left(-2\left(\theta+\epsilon_{\theta}\right)\right)\mathbf{M_{H}}\mathbf{M_{rot}}\left(2\left(\theta+\epsilon_{\theta}\right)\right)\mathbf{M}_{\delta}\left(\delta+\epsilon_{\delta}\right)\mathbf{M_{matter}}\mathbf{S_{S\rightarrow P}} \tag{3.20}$$

For each of the intensities incident on the detector, the value of the intensity will change depending on e, ϵ_{θ}, and ϵ_{δ}. To observe the absolute error, the Mueller matrix representing the solution is assumed to be identity. The intensities for each beam are described here and each degenerate output from the analysers will be observed. The error is assumed to be slight and centred around zero, so a first order Taylor approximation is taken for each measured intensity on the detector.

For this analysis, the intensity on the detector can be formulated as

$$\mathbf{I_{D}}=\mathbf{A}\mathbf{M_{analyser}}\mathbf{S_{M\rightarrow A}} \tag{3.21}$$

where $\mathbf{M_{analyser}}$ can be split into the ideal matrix and the first order approximation of the error

$$\mathbf{I_{D}}=\mathbf{A}\left(\mathbf{M_{analyser}}+\mathbf{M_{error}}\right)\mathbf{S_{M\rightarrow A}} \tag{3.22}$$

where $\mathbf{M_{error}}$ is Mueller matrix of error. This can be expanded to

$$\mathbf{I_{D}}=\mathbf{A}\mathbf{M_{analyser}}\mathbf{S_{M\rightarrow A}}+\mathbf{A}\mathbf{M_{error}}\mathbf{S_{M\rightarrow A}} \tag{3.23}$$

The term on the right will contain only the impact of first order approximation of the error on $\mathbf{I_{D}}$. To make this analysis input Stokes vector ambiguous, only $\mathbf{AM_{error}}$ is analysed. The resulting matrix will have all zero entries, but the top row. In the following analysis, we will look on at the top row of $\mathbf{AM_{error}}$ as a vector called **E'**.

Horizontal Analyser In the case of the horizontal analyser, all the error that emerges will be linear with respect to e.

$$\mathbf{E'} = \begin{pmatrix} \frac{1}{2}e & -\frac{1}{2}e & 0 & 0 \end{pmatrix} \tag{3.24}$$

The above vector demonstrates that for the Stokes vector of the light beam that emerges from the solution, the error will scale proportional to half the extinction coefficient for the S_0 and S_1 terms. For the degenerate case of horizontally polarised light, there is no error in the incident intensity.

Vertical Analyser Similarly for the vertical analyser, all the error that emerges will be linear with respect to e.

$$\mathbf{E'} = \begin{pmatrix} \frac{1}{2}e & \frac{1}{2}e & 0 & 0 \end{pmatrix} \tag{3.25}$$

Similar to the prior case, but here there will be no error in the degenerate case of input vertically polarised light.

+45° Analyser This is a rotated analyser and from the Mueller matrices formulated in this section, there is potential error from the angular placement of the analyser and from the imperfect diattenuation of the polariser.

$$\mathbf{E'} = \begin{pmatrix} \epsilon_\theta & -\frac{1}{2}e & \frac{1}{2}e & 0 \end{pmatrix} \tag{3.26}$$

In this case, the intensity of the beam itself is influenced by the error in the angular placement of the horizontal filter and, unlike the other cases, the error from the polariser influences the second and third Stokes parameter. In the degenerate case of +45° light however, the error from the polarisers persists. The cause of this is the use of a first order Taylor approximation on the cos and sin functions.

Right-hand Circularly Polarised Analyser All the same error sources from the prior analyser exist, but there is also an error in the phase change incurred by the retarder.

$$\mathbf{E'} = \begin{pmatrix} e & \epsilon_\theta & \frac{1}{2}\epsilon_\delta & \frac{1}{2}e \end{pmatrix} \tag{3.27}$$

For analysing RHCP, we notice that there is twice the error incurred from the linear polariser on the intensity of the beam. In this case, similar to the case above, the error persists in the degenerate case of RHCP light.

3.4 Summary

In this chapter, we have proposed the design of an inexpensive, compact polarimeter. This polarimeter uses an amplitude division method using a single illumination source with a train of beamsplitters and ND filters to reduce quantisation error in the measurements. The light beams produced from the beamsplitters are passed through an apparatus that has filters holders for polarising elements and analysers and secures a cuvette of solution, thereby reducing alignment errors. After which, the beams come into contact with a detector.

In prior chapters, we have alluded to possible intensity variations that can occur in the $\mathbf{A}$ matrix, causing then to vary from ideal intensities. In the next chapter, we look to enhance those measurement to make them closer to the ideal using a spatial detector array.

Chapter 4

Computational Enhancement

Noise comes from the physical characteristics of the light source being used and from the electronics involved in the measurement and is an inherent problem in polarimetric measuring systems. Conventional methods for reducing noise have been to manipulate the arrangement of optical elements or to perform Time Averaging of the measured signal from a photodiode.

One of the main contributions of this thesis is the use of computational enhancement methods that take advantage of the full spot size incident on a spatial detector. This mimicking of temporal multiplexing using a single spatial acquisition allows for faster acquisitions of polarimetric measurements. This section will outline two ways in which spatial enhancement techniques can be used to improve polarimetric measurements. But first, we will come up with a theoretical model of the observed intensity, $\mathcal{U}$, incident upon the detector from its ideal intensity, $\mathcal{I}$.

All the methods outlined in this chapter will be compared in Chapter 5 and Chapter 6.

4.1 Pixel Intensity Model

Before any method for computational enhancement is hypothesised, we need to model the observed intensity as a function of the ideal. Since we are moving from a single measurement through time to a set of measurements in space, we redefine variables used in Section 2.3.2. Our observed intensity $\mathcal{U}$, ideal intensity $\mathcal{I}$, and enhanced intensity $\hat{\mathcal{U}}$ are now defined as sets of measurements. Since these measurements are susceptible to variation, the

members of these sets are called random variables. For the sake of maintaining convention, the members of $\mathcal{I}$ will be v:

$$\mathcal{I} = \{v_0, ..., v_i, v_j, ..., v_n\} \tag{4.1}$$
$$\mathcal{U} = \{u_0, ..., u_i, u_j, ..., u_n\} \tag{4.2}$$
$$\hat{\mathcal{U}} = \{\hat{u}_0, ..., \hat{u}_i, \hat{u}_j, ..., \hat{u}_n\} \tag{4.3}$$

where subscript i, j represent the index of any two random variables of the set. In Section 2.3, we identified two sources of noise that can influence the measured intensity on the detector: physical intensity variations (i.e., shot noise and speckle) and electrical noise (i.e., amplifier read-out noise). Our model should incorporate these noise sources; therefore, we can follow the work from Boulanger *et al.* [26]. This work models the observed intensities as

$$u_i = g_0 z_i + \eta \tag{4.4}$$

where z_i is the Poisson degraded value of v_i, g_0 is the gain applied on the signal, and η is a value sampled from a zero-mean Gaussian process (i.e., $\eta \sim \mathcal{N}(0, \sigma)$). The degradation from shot noise is modelled as a Poisson process with a variance that is signal-dependant. Any enhancement method that accounts for shot noise can either: i) incorporate Poisson statistics directly into the enhancement algorithm [27] or, ii) treat the enhancement in a modular fashion using variance stabilisation [28]. Both these algorithms work to similar effect, however, the first limits the range of enhancement methods to those that specifically account for shot noise. The second method stabilises the variance of the noise to the be independent of the signal intensity. This allows for the use of the many enhancement methods that assume constant variance.

Considering shot noise into the pixel model can lead to better enhancement in cases where there is a low number of incident photons [27], however, the device built in this thesis is capable of illuminating the detector with a large number of photons. This high incidence of photons allows for the Poisson process to be approximated as having a Gaussian distribution. This approximation is demonstrated in Appendix A. There are some cases where there will be a low number of incident photons, for example, if there is high amount of scattering from the solution, or if there is a low measured intensity of a polarisation state, but we will be excluding those cases from the scope of this thesis.

With the approximation of the shot noise as a Gaussian, our pixel model will follow the same model as in eq. 2.82

$$u_i = v_i + \eta \tag{4.5}$$

where v_i is the ideal intensity signal incident on the detector, and η is a value sampled from a zero-mean Gaussian process (i.e., $\eta \sim \mathcal{N}(0, \sigma)$). Special note has to be taken here due to what we are measuring. The objective of this system is to measure the polarimetric state of a light beam. An analyser filters a state of that beam, but the analysers are not perfect and there can be an intensity influence from other polarisations in the light beam. To this end, we have to modify our interpretation of $\mathcal{I}$ to being the ideal intensity of the light beam with some deterministic error.

$$\mathcal{I} \sim \mathcal{I} + \mathcal{E} \tag{4.6}$$

We have described a model that is capable of describing the measured intensity out of the detector as it is varied through noise processes and deterministic error created from the use of inexpensive, commercial-grade polarisers. In the next sections, we will describe two methods that will use the full spatial detector array as independent measurements to enhance the polarimetric measurements $\mathcal{U}$ to produce measurements similar to the ideal measurement of the polarised state of the light beam ($\hat{\mathcal{U}} \sim \mathcal{I}$).

4.2 Model Fitting

One of the benefits of using a spatial detector array is that we can use the spatial intensity arrangement of the incident laser spot as a basis for comparison to an ideal laser spot. This difference in intensity can offer insight into the intensity variations in the systems and losses due to the scattering from the solution. The assumption is that there is a uniform intensity loss across the entire laser spot due to scattering. With the use of the ideal laser spot as a model and certain noise assumptions, that will be discussed later, we can use this ideal model to enhance the measurements.

We shall call the ideal spot pattern on the spatial detector array $\mathcal{L}$, defined as the set of spatial intensities in eq. 4.7.

$$\mathcal{L} = \{l_0, ..., l_i, l_j, ..., l_n\} \tag{4.7}$$

The objective of this method is to maximise the likelihood that the set of random variables representing our measurements $\mathcal{U}$ resemble $\hat{\mathcal{L}}$, $P(\mathcal{U}|\hat{\mathcal{L}})$, where $\hat{\mathcal{L}}$ is a transformed set of the ideal measurements, modelled by

$$\hat{\mathcal{L}} = \alpha\mathcal{L} - C \tag{4.8}$$

where α is a scaling factor, C is an intensity bias and the members of $\hat{\mathcal{L}}$ are

$$\hat{\mathcal{L}} = \{\hat{l}_0, ..., \hat{l}_i, \hat{l}_j, ..., \hat{l}_n\} \tag{4.9}$$

To ensure a realistic fit and avoid any trivial cases, we apply some constraints to these parameters:

1. $\alpha > 0$
2. $C > 0$
3. $\hat{l}_i > 0 \, \forall \, i \in \hat{\mathcal{L}}$

Given the model defined in eq. 4.8, we can reformulate our objective as trying to maximise the probability of the measurements occurring given a set of parameters, $\underline{\theta}$.

$$\underline{\theta} = \underset{\underline{\theta}}{\operatorname{argmax}} \, P\left(\mathcal{U}|\underline{\theta}\right) \text{ where } \underline{\theta} = \begin{pmatrix} \alpha \\ C \end{pmatrix} \tag{4.10}$$

To properly define this probability, we need to make some assumptions. For this problem, we shall assume the random variables in $\mathcal{U}$ are independent and identically distributed (iid) and we shall assume there is only the zero-mean Gaussian noise coming from the detector to vary the measurements. To this end, we model the likelihood as a normal distribution centred around a biased, scaled $\mathcal{L}$. We will use the iid assumption to further model the likelihood as

$$P\left(\mathcal{U}|\underline{\theta}\right) = \prod_{i=0}^{n} p\left(u_i|\underline{\theta}\right) \tag{4.11}$$

where

$$p\left(u_i|\underline{\theta}\right) = \exp\left[-\frac{\left(u_i - \left(\alpha l_i - C\right)\right)^2}{\sigma}\right] \tag{4.12}$$

We can take the logarithm of both sides of eq. 4.11, resulting in eq. 4.13.

$$\log P\left(\mathcal{U}|\underline{\theta}\right) = -\sum_{i=0}^{n} \frac{\left(u_i - \left(\alpha l_i - C\right)\right)^2}{\sigma} \tag{4.13}$$

Since σ will be constant over all the random variables due to the iid assumption, we can disregard it and reformulate our problem to minimising instead the cost function $\mathcal{C}\left(\theta\right)$, defined in eq. 4.14.

$$\mathcal{C}\left(\underline{\theta}\right) = \sum_{i=0}^{n} \left(u_i - \left(\alpha l_i - C\right)\right)^2 \tag{4.14}$$

and once the parameter set is found, the enhanced measurements, $\hat{\mathcal{U}}$, will be equal to the scaled and shifted version of $\mathcal{L}$, $\hat{\mathcal{L}}$.

$$\hat{\mathcal{U}} = \hat{\mathcal{L}} \tag{4.15}$$

4.3 Spatial Filtering

The Model Fitting mentioned above is an optimization method which compares all the measured intensities to all the ideal spot size measurements. This method, while being elegant and straightforward, can only be performed if the ideal spot is known *a priori* and the assumption of maintained coherence can be applied after the laser has passed through the solution. In cases where that assumption cannot be used, we have to use the measurements alone to produce the set of enhanced measurements. To do this, we look to a field where spatial detector arrays are common: image processing.

A common assumption in the field of image processing is that there is some homogeneity in intensity between a detector pixel and its' surrounding neighbours. The pixels on a detector are small enough and the modulation in intensity on the laser spot is 'smooth' enough that we can apply this assumption here to enhance the measurements on the spatial detector array. The use of this assumption allows us to use a similar method for measurement enhancement as in eq. 2.18, except over a spatial neighbourhood, rather than time. And, just like in eq. 2.18, we are assuming the noise is sampled from a zero-mean Gaussian distribution.

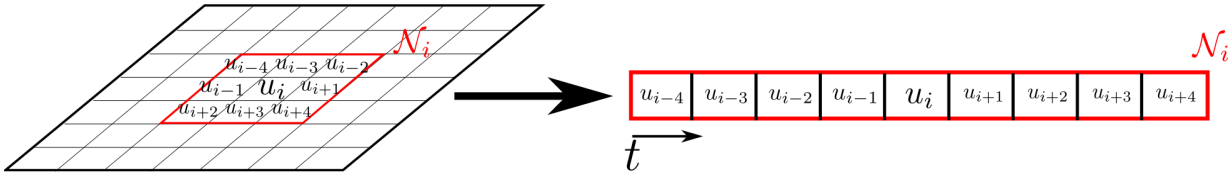

Figure 4.1: Graphical similarity between averaging over a spatial area and over time.

$$\hat{u}_i = \frac{1}{N} \sum_{j \in \mathcal{N}_i} u_j \tag{4.16}$$

where $\mathcal{N}_i$ is the surrounding neighbourhood of detector pixels around pixel i and N is the number of pixels in $\mathcal{N}_i$. The difference between eq. 4.16 and eq. 2.18 is that we are not summing over all measurements, we are only summing over the measurements in a local area. A similarity can be drawn between the two, where if we take the pixels over the local area and arrange them as a one dimensional vector, like in Figure 4.1, they mimic measurements taken through time.

This spatial homogeneity assumption has its' limitations, primarily edges and high frequency textures. Edges are abrupt spatial changes in intensity and when they occur inside the neighbourhood of u_i, they can cause smearing to occur when using the Spatial Averaging method. Spatial Averaging has no discrimination between high frequency intensities and noise, so in regions where there are high frequency interference patterns, Spatial Averaging will homogenise the intensities. There are more advanced Spatial Averaging algorithms that try to account for these abrupt and high frequency changes in ideal measurement intensity, however, they are outside the scope of this thesis.

Due to the use of imperfect optical elements, we ideally want to use an illumination source that can suppress any other noise sources. The use of a powerful illumination source also has the benefit of amplifying any low intensity polarisation states. With the use of this illumination source, the shot noise will take on a Gaussian shape, and we will use this assumption in the later Chapters 5 and 6. A consequence of using a powerful illumination source is that the **E'** vectors mentioned in Section 3.3 become amplified. However, in all these algorithms, once the system is modelled and the noise has been suppressed, the imperfections in the system can be accounted for using the imperfect Mueller matrices from Section 3.3.

4.4 Summary

In this chapter, we have produced a model of the measured light intensity from a spatial detector array pixel, taking into account the deterministic error from optical elements and electrical noise. We make an important assumption here that the incoming flux of photons is large enough that we can assume the shot noise takes a Gaussian shape. This allows us to make Gaussian noise assumptions in our formulations.

To enhance these measured intensities, we propose two methods that utilise the full set of measurements from a spatial detector array. One method reconstructs the system from an ideal model, known *a priori* and the other uses an assumption of local intensity homogeneity on the detector to perform Spatial Averaging. This method was shown to have some similarity with the Temporal Averaging method.

Chapter 5

Synthetic Experiment

In the prior chapters, we introduced a design for and built an inexpensive, compact polarimeter and a novel method for polarimetric measurement and enhancement. We use the combination of the main contributions, in this chapter and the next, to estimate the concentrations of sugar in a solution. The results are summarised here and in the next chapter. We will first test this system under synthetic conditions in this chapter and then under real conditions in the next.

To demonstrate the capabilities of this thesis' contributions, we perform two tests. The first test will use a simulated detector with four light beams representing the four polarisation states incident on the detector. The second test will enhance the measurements taken through a cuvette of sugar solution. This chapter will outline the experimental setup for performing the synthetic experiments, the experimental results and the quantitative metrics used to evaluate those results.

5.1 Experimental Setup

The purpose of the synthetic experiment is to the validate the performance of our measurement enhancement methods on synthetic data with known ideal characteristics to estimate the concentration of sugar in the solution. To this end, we start with a laser spot, shown in Figure 5.1. The ideal laser spot is a sinusoidally modulated ellipse mimicking real laser spots seen using coherent laser sources.

This light beam will pass through a solution of chiral molecules that will rotate it by a certain degree that is proportional to the concentration of those chiral molecules in a

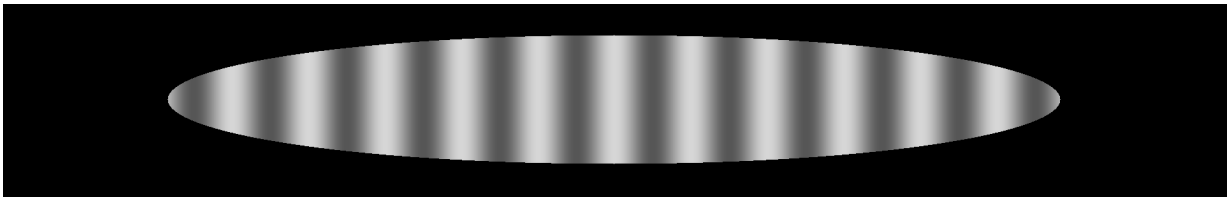

Figure 5.1: Simulated laser spot on the spatial detector array.

clear solution. This has been theoretically modelled by Biot's Law, which states that the amount of rotation that linearly polarised light undergoes is equal to

$$\theta = [\alpha]_{\lambda}^{T} \, cl \tag{5.1}$$

where c is the concentration of the sugar in the solution in $\left[\frac{\text{g}}{\text{ml}}\right]$, l is the pathlength in decimeters (10 cm, dm), $[\alpha]_{\lambda}^{T}$ is the specific rotation in $\left[\text{degg}^{-1}\text{dm}^{-1}\right]$ and θ is the observed rotation in polarisation in degrees [29]. We will keep this experiment solution-agnostic at this point. The degrees of rotation tested are summarised in Table 5.2. For this synthetic experiment, we will incorporate the non-ideal characteristics in commercial-grade linear polarisers. We will not use the errors that can be encountered through the use of retarders or in the placement of the rotated linear polariser for this experiment.

We will be assuming that the light is vertically polarised before encountering the solution and as a result the intensities incident on the detector can be modelled as

$$\begin{pmatrix} I_H \\ I_V \\ I_{+45^\circ} \\ I_{RHCP} \end{pmatrix} = \frac{1}{4} \begin{pmatrix} (e_1+1)(e_2+1) - \cos(2\theta)(e_1-1)(e_2-1) \\ (e_1+1)(e_2+1) + \cos(2\theta)(e_1-1)(e_2-1) \\ (e_1+1)(e_2+1) + \sin(2\theta)(e_1-1)(e_2-1) \\ (e_1+1)(e_2+1) - \sin(2\theta)(e_1-1)(e_2-1) \end{pmatrix} I_o \tag{5.2}$$

where I_H, I_V, I_{+45°, and I_{RHCP} are the intensities for the four spots (horizontally, vertically, $+45^\circ$ and RHCP polarised, respectively) representing measurement profiles incident on the detector and I_o is the intensity of the ideal laser spot. This description is not complete since there will be some transmission loss from the use of commercial polarisers, so eq. 5.2 is actually

$$\begin{pmatrix} I_H \\ I_V \\ I_{+45^\circ} \\ I_{RHCP} \end{pmatrix} = \frac{1}{4} \begin{pmatrix} (e_1+1)(e_2+1) - \cos(2\theta)(e_1-1)(e_2-1) \\ (e_1+1)(e_2+1) + \cos(2\theta)(e_1-1)(e_2-1) \\ (e_1+1)(e_2+1) + \sin(2\theta)(e_1-1)(e_2-1) \\ (e_1+1)(e_2+1) - \sin(2\theta)(e_1-1)(e_2-1) \end{pmatrix} \bar{I}_o \tag{5.3}$$

Table 5.1: Table of Specifications for the Point Grey GS3-U3-236M-C camera where fps is the maximum possible readout of frames per second, e^- represent electrons and ADU is the detector units represented out of 16-bits.

Camera Parameter	Value	Units
Frames per sec	128	fps
ADC	12	bits
Shutter Speed	0.035	ms
Gain	0.52	e^-/ADU
Temporal Dark Noise	6.68	e^-
QE @ 635 nm	55	%

where $\bar{I}_o$ is the attenuated ideal intensity from the laser due to transmission losses. We will assume that there is 25% transmission in the linear polarisers. Using the setup outlined in the next chapter, we will assume that there is 25% transmission in the linear polarisers and that $e_1 = 1/9000$ and $e_2 = 1/1000$. To calculate the angle of rotation from the intensities above, we can invert one of the intensities to solve for θ. For this experiment, we shall invert I_V using eq. 5.4.

$$\theta = \cos^{-1}\left(\frac{\frac{4I_V}{\bar{I}_o} - (e_1+1)(e_2+1)}{(e_1-1)(e_2-1)}\right) \tag{5.4}$$

To mimic the noise conditions that can occur during real measurements, mentioned in Section 2.3.1 and 2.3.2, we look to utilize the industry specifications of spatial detector arrays as a starting point. For this, we choose the Point Grey GS3-U3-236M-C camera (Point Grey, Canada) whose specifications are summarised in Table 5.1. Example of a noisy measurement profiles are in Figure 5.2. We used a laser at 0.375mW and the parameters in Table 5.1. The profiles in this figure have been magnified to demonstrate the occurring noise.

To vary the noise that can occur in these images, we modify the incident photon flux by changing the power of the laser, thereby influencing the amount of shot noise, and we can modify the variance of the temporal noise. The testing values are summarised in Table 5.2. We will choose the maximum laser power that can be incident on the detector without saturating the pixels. We look to Table 5.1 to find that 0.375mW is the maximum amount, so we choose to have our simulations incur a laser power in multiples of 0.375mW. The range of temporal noise values is sampled from the CMOS detector product line from Point Grey (Point Grey, Canada).

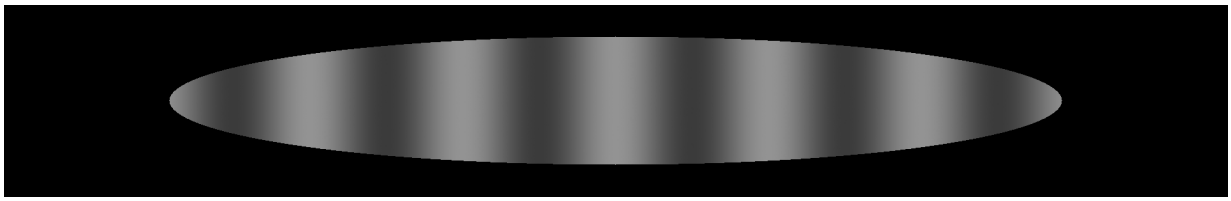

(a) Power: 0.375 mW, Dark Noise: 21 e^-

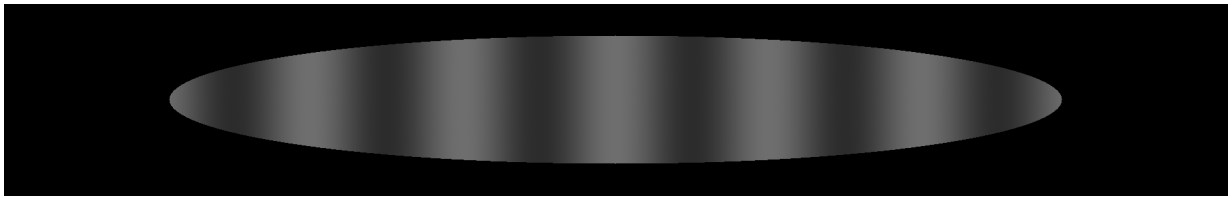

(b) Power: 0.281 mW, Dark Noise: 18 e^-

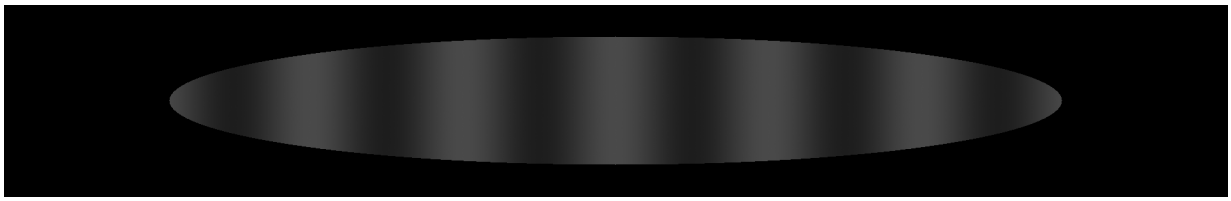

(c) Power: 0.188 mW, Dark Noise: 15 e^-

(d) Power: 0.094 mW, Dark Noise: 21 e^-

Figure 5.2: Simulated measurement profiles of the vertical intensities incident upon the detector under the assumption of no depolarisation. These profiles have been contaminated with noise at various power levels and noise amounts specified in Table 5.1.

Table 5.2: Table to summarise the range of values used for the simulation experiment.

Parameter	Testing Range	Interval
Laser Power Scale	0 – 1	0.25
Temporal Noise	0 e^- – 30 e^-	6 e^-
Rotation	0 ° – 15°	3°

Table 5.3: Averaging algorithm parameters for simulated experiments.

Algorithm	Parameters
Spatial Averaging	$\mathcal{N} = 3 \times 3$ pixels
Temporal Averaging	$N = 9$ frames

5.2 Algorithm Parameters

We enhanced the measurements using the three methods mentioned in this thesis: Temporal Averaging from Section 2.3, Spatial Averaging from Section 4.3 and Model Fitting from Section 4.2. Model Fitting requires a model to enhance the measurements, so the intensities calculated in eq. 5.3 will be its' model. The Temporal Averaging algorithm will take a single pixel location in the simulation image and average its value through N temporal acquisitions, where N is the same number of pixels included in the Spatial Averaging algorithm's homogeneous assumption ($\mathcal{N}$). The reason for this choice of N is to properly perform the comparison of a Spatial Averaging to Temporal Averaging for polarimetric measurement enhancement. The parameters for spatial and Temporal Averaging are summarised in Table 5.3. The $\mathcal{N}$ was found by finding the size which maximises the peak-signal-to-noise (PSNR) metric over all the parameters in Table 5.2. For demonstration purposes, a measurement profile is shown where all the pixels have been time averaged independently, however, the values for PSNR and angle will still be calculated using a single pixel.

5.3 Quantitative Evaluation

The performance of the spatial enhancement methods will be gauged against the original contaminated noise profile and the state-of-the-art measurement enhancement method of Time Averaging. For this comparison, the metric of PSNR is used, defined as

$$\text{PSNR} = 20 \log_{10} \left(\frac{MAX_I}{\sqrt{MSE}} \right) \tag{5.5}$$

where MAX_I is the maximum value possible on the detector and MSE is the mean squared error between the ideal measurement profile and the enhanced one. To reduce quantisation error, we simulate a 16-bit detector, so $MAX_I = 2^{16}$. A high PSNR implies the enhanced

Table 5.4: Average values for PSNR and angular estimation from the temporal and spatial algorithms for measurement enhancement.

Algorithm	PSNR(dB)		$\lvert\Delta\theta^\circ\rvert$	
	Mean	Std	Mean	Std
No Enhancement	70.19	5.53	0.5025	0.7534
Temporal Averaging	102.69	0.30	0.0718	0.1239
Model Fitting	**121.16**	9.47	**0.0230**	0.0514
Spatial Averaging	79.35	5.11	0.2781	0.4704

measurements have a strong resemblance to the ideal measurement profile, while a low PSNR implies a large difference between the enhanced and ideal profiles.

We will also compare the estimates for the angle of rotation caused by the chiral solution using an absolute difference between the algorithm's estimate and the known rotation

$$|\Delta\theta| = |\theta_{actual} - \theta_{calc}| \tag{5.6}$$

where θ_{actual} is the angle sampled from Table 5.2 and θ_{calc} is the angle estimated from the enhanced profiles. The smaller this metric, the better.

5.4 Observations

In this section, we will demonstrate the performance of spatial algorithms on a synthetic laser spot, which has been contaminated with shot and dark noise, in estimating the angular rotation of linearly polarised light.

For comparison across all parameters, we compare the mean and standard deviation of the PSNR and θ difference metrics. These results are summarised in Tabel 5.4. The tables of results for each set of test parameters are in Appendix B. To visually compare the spatial algorithms alone, we place them side-by-side with their ideal and noisy counterparts to observe the measurement enhancement potential of these algorithms for a set of test parameters. This is done in Figure 5.3.

From Table 5.4, we can see that Model Fitting and Temporal Averaging perform comparably in terms of PSNR, while Spatial Averaging does not produce as high a PSNR value. However, it is still higher than if there was no enhancement applied and allows us

Table 5.5: Concentration differences due to error in angular measurement using all three algorithms. Lowest average difference is bolded.

Algorithm	$\lvert\Delta\theta^\circ\rvert$		Maltodextrin $\lvert\Delta c\rvert \frac{g}{ml}$		Glucose $\lvert\Delta c\rvert \frac{g}{ml}$	
	Mean	Std	Mean	Std	Mean	Std
No Enhancement	0.5025	0.7534	0.0276	0.0414	0.0954	0.1430
Temporal Averaging	0.0718	0.1239	0.0039	0.0068	0.0136	0.0235
Model Fitting	**0.0230**	0.0514	**0.0013**	0.0028	**0.0044**	0.0098
Spatial Averaging	0.2781	0.4704	0.0528	0.0893	0.0153	0.0258

to conclude that spatial methods can reduce the intensity variations that come from imperfections in the system and noise. The reason for the performance of Spatial Averaging is likely due to the failures in the spatial intensity homogeneity assumption at the edges of the measurement profile and the background.

Model Fitting is able to estimate the rotation angle with higher accuracy and precision than Temporal averaging. We observe the implications of this by determining the concentration of two faux sugar solutions. One solution will have an optical activity of 52.7 (similar to that of D-glucose [30]) and the other will have an optical activity of 181.97 (similar to that of Maltodextrin DE 17 [31]), which we call Glucose and Maltodextrin, respectively. The pathlength used will be 0.1 dm. We reformulate eq. 5.1 to be in difference form and solve for $|\Delta c|$

$$|\Delta c| = \frac{|\Delta\theta|}{[\alpha]_\lambda^T \, l} \tag{5.7}$$

In Table 5.5, we see that Model Fitting is capable of estimating the concentrations with more accuracy and precision than the other enhancement methods. Spatial averaging does not produce as accurate or precise results, but is still a better estimation than no enhancement. The error in the estimation from Model Fitting and Temporal Averaging are in the thousandth of grams per millilitre. Depending on the application, these errors can be negligible, or quite troublesome.

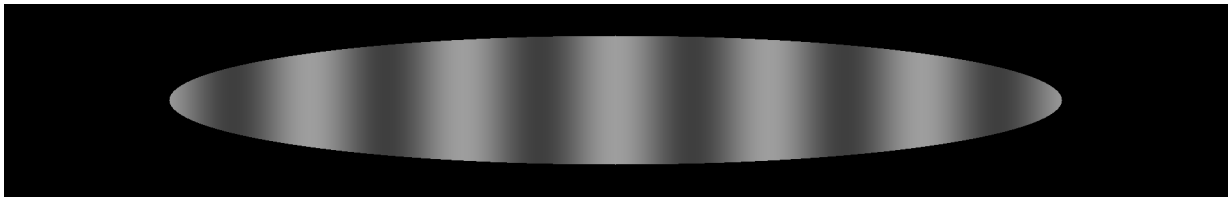

(a) Ideal Measurement Profile from Source

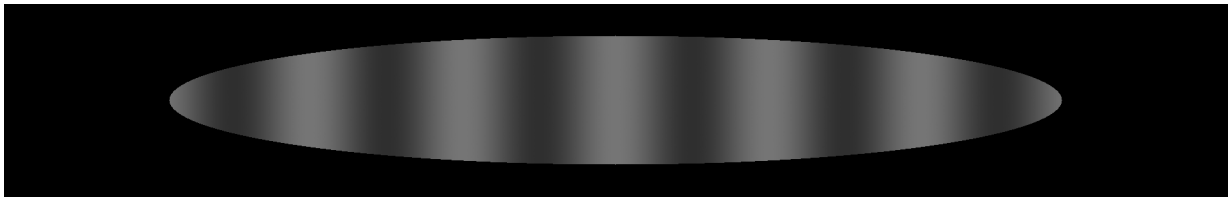

(b) Noisy Rotated Measurement Profile

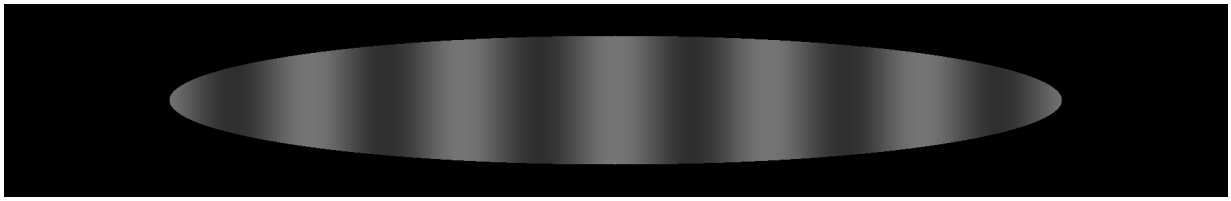

(c) Model Fitting

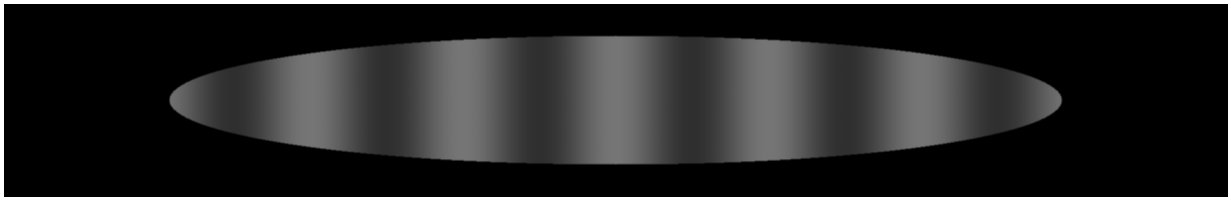

(d) Spatial Averaging

Figure 5.3: Side-by-side comparison of the enhanced measurement profiles from spatial algorithms.

Chapter 6

Real Experiment

We used the inexpensive, compact polarimetry system to estimate the concentration of Maltodextrin DE 16.5-19.5 (Sigma-Aldrich, MO) in a clear solution. After measurements have been taken with the system, we apply the better performing of the two spatial algorithms used in the previous chapter, Model Fitting, to enhance the measurements. We then compare the theoretical results following Boit's law to the measurements before and after enhancement. The objective of this experiment is to validate the performance of a spatial enhancement method in a real scenario.

6.1 Experiment Setup

For this experiment, we decomposed the device into using a single polarising element and analyser. This is shown in Figure 6.1. Solidworks parts in the rendering were provided by Thorlabs, Inc. (Thorlabs, NJ). The light source is a 635 nm, 5 mW laser. The filter holder part in this configuration will contain the NE2R20B (Thorlabs, NJ) ND filter which will transmit a 635 nm light beam with 0.1% of it's full power. The polarising filter holder in the cuvette analyser will contain a single high contrast polarising film from Edmund Optics, Inc. (Edmund Optics, NJ) arranged vertically, with a transmission of 42%. The analysing filter holder in the cuvette analyser will be empty; replaced with a rotating nanoparticle linear film polariser from Thorlabs, Inc (Thorlabs, NJ), with a transmission of 80%. We will use this as a vertical polariser for capturing the measurement profile. The cuvette holding the sugar solution is a UV Fused Quartz cuvette (CV10Q3500) (Thorlabs, NJ) with physical outer dimensions of $12.5 \times 12.5 \times 45$ mm, inner dimensions of $10 \times 10 \times 44.75$ mm and a fluid capacity of 3.5 mL. This provides a pathlength of 0.1 dm through the

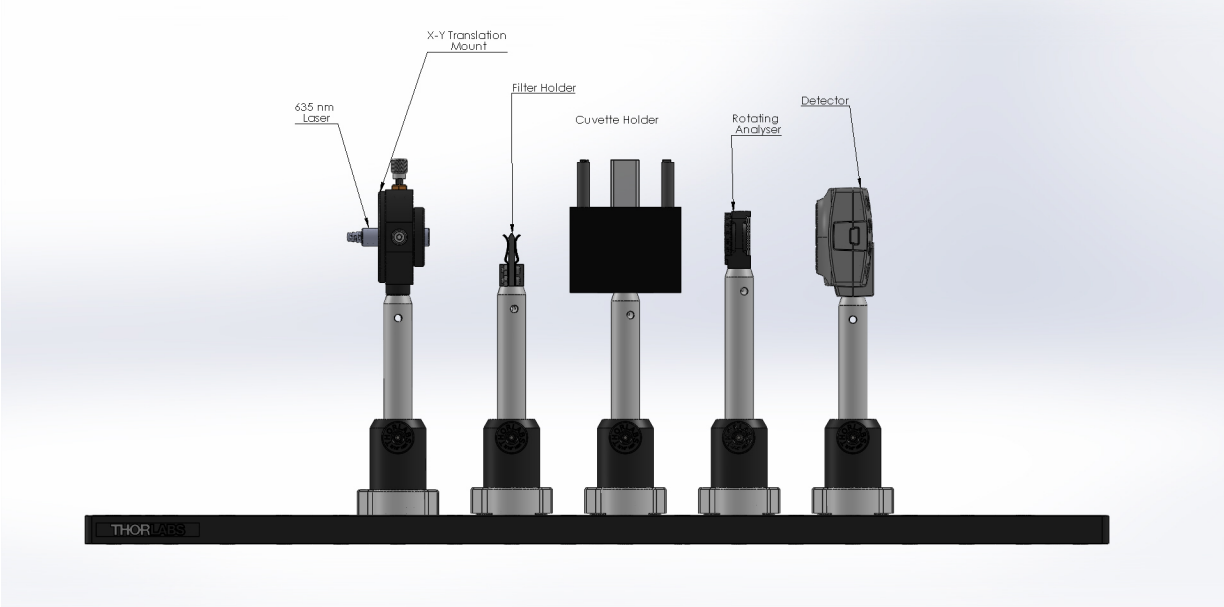

Figure 6.1: Experimental setup for the Real experiment to determine sugar concentrations.

solution. The detector in this setup will be the same detector that we used as a basis in our synthetic experiments. The parameters for that detector are summarised in Table 5.1.

We will use the same model we used in our synthetic experiments, eq. 5.3, to describe the incident intensity of the vertically polarised state

$$\mathbf{I} = \left(\frac{(1 + e_{V_1})(1 + e_{V_2})}{4} + \frac{(e_{V_1} - 1)(e_{V_2} - 1)\cos 2\theta}{4} \right) \bar{\mathbf{I}}_\mathbf{b} \tag{6.1}$$

where $\mathbf{I_b}$ is the vector of beam intensities from eq. 3.4.

In the current system, the vertical polariser in the filter holder has an extinction ratio of $e_{V_1} = {}^1/_{9000}$ and the rotating analyser has an extinction ratio of $e_{V_2} = {}^1/_{10000}$. In addition to the error caused by the optical elements, there is a scaling factor attributed to the transmission loss in the overall intensity as the light beam passes through each element. According to the specifications for each of these elements, the vertical polariser will have a 42% transmission and the rotating analyser with have an 80% transmission, thereby making $\mathbf{I_b}$ into a scaled $\bar{\mathbf{I}}_\mathbf{b}$. This transmission loss is assumed uniform, thereby not making it a source of error and rather a calibration factor.

6.2 Experiment Parameters

To demonstrate the capabilities of the system to estimate sugar concentrations in solution, we use Maltodextrin DE 16.5-19.5 at 0.824 $\frac{g}{ml}$ with an optical activity of 181.97 [31].

6.3 Procedure

The procedure that we will follow for this experiment is outlined in this section. Before the experiment begins, calibration of the system needs to occur. The calibration procedure has two steps:

1. Identifying fixed pattern noise
2. Capturing the ideal laser spot pattern scattered through a control solution

Fixed pattern noise can be determined by taking multiple exposures in a constant illumination environment (i.e., having the intensity flux incident on the detector uniform) and time averaging each pixel independently on the detector. This allows for the zero-mean Gaussian dark current to approach zero, leaving only noise that can occur due to constant inhomogeneities between the pixels in the detector. And since these inhomogeneities are constant, a constant offset can be applied to each measurement profile we capture to remove these artefacts.

To apply the Model Fitting method discussed in the previous chapter, we need to capture the laser profile on the detector. Since there is a high chance that the laser will lose some coherence as it passes through a solution, we capture the laser profile after it travels through a control solution (i.e., a solution with no chiral molecules) and use this as our model to enhance our measurements. By doing this, that loss of coherence is mimicked to some degree.

After the calibration procedure has finished, we then proceed to capturing the measurement profiles. We capture 300 exposures of the laser profile. Each exposure will be spatially enhanced independently to find the precision of our estimation. We will report the mean and standard deviation in the estimation error from all 300 exposures.

Table 6.1: Summary of the difference between the theoretical and calculated angles after measurement enhancement.

Theoretical Angle	Estimated Angle		$\lvert\Delta\theta^\circ\rvert$		$\frac{\lvert\Delta\theta\rvert}{\lvert\theta\rvert}$
	Mean	Std	Mean	Std	
14.99	15.28	0.05	0.28	0.05	0.02

6.4 Evaluation

Unlike the synthetic experiments outlined in the last chapter, there is no ideal measurement to compare against after enhancement(i.e., no PSNR metric), so we will use the model outlined in eq. 5.1 as the benchmark. We take the pathlength given by the cuvette in the optical system and the concentration and optical activity from Section 6.2 to calculate the ideal rotation angle caused by the chiral molecules in the solution. That angle is 14.99 degrees.

The rotation angle from the measured intensity profile will be calculated by using the ratio of the maximum intensity in the enhanced measurement profile to the original measurement profile of the light beam, captured during our calibration procedure and then solving for θ using eq. 5.4. The correctness of our enhancement will be evaluated as the absolute difference between the rotation angle calculated from the enhanced measurement, θ_{em}, and the theoretically obtained angle, θ_{calc} (eq. 6.2). The smaller the difference, the better the enhancement.

$$|\Delta\theta| = |\theta_{em} - \theta_{calc}| \tag{6.2}$$

6.5 Observations

This section will demonstrate the results of using spatial enhancement algorithms for determining the concentration of a chiral molecule in a a clear solution. This solution has a concentration of 0.824 $\frac{\text{g}}{\text{ml}}$ of Maltodextrin DE 16.5-19.5. We compare the theoretical and calculated angles in Table 6.1, show the spatial measurement profiles in Figure 6.2, and the resulting spatial angular profile in Figure 6.3. To determine the final angular rotation, we take a small area in the centre Figure 6.3 and use its' average.

In Figure 6.2, we see that there are interference effects from the crystallised sugar in the solution and through the use of Model Fitting, these intensity variations were corrected, unintentionally. If a single point measurement was used and the interference pattern of

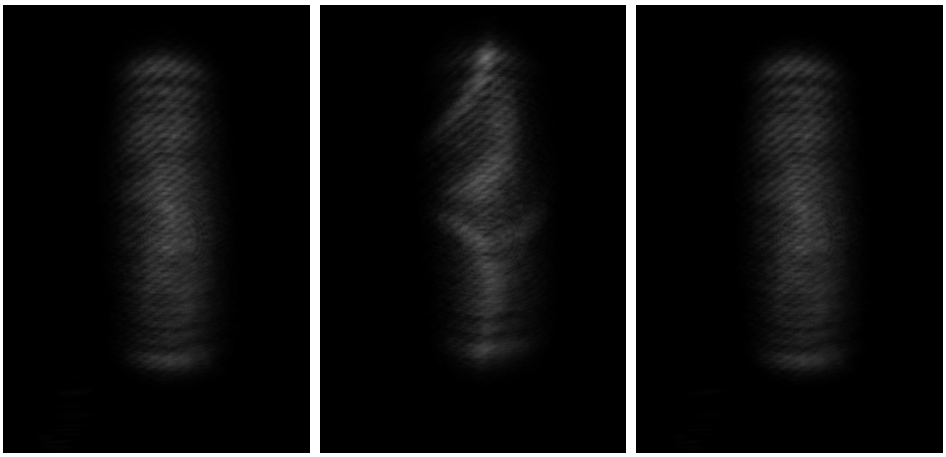

(a) Ideal (b) Measured (c) Enhanced

Figure 6.2: The measurement profiles of the light beam through a control solution, the noisy measurements of the light beam through Maltodextrin and the enhanced measurement profile, enhanced through Model Fitting, used to determine the spatial angular profile.

Table 6.2: Summary of the difference between the actual and calculated concentrations after measurement enhancement.

Actual Concentration	Estimated Concentration		$\lvert\Delta c\rvert$		$\frac{\lvert\Delta c\rvert}{\lvert c\rvert}$
	Mean	Std	Mean	Std	
0.824	0.839	0.002	0.015	0.002	0.019

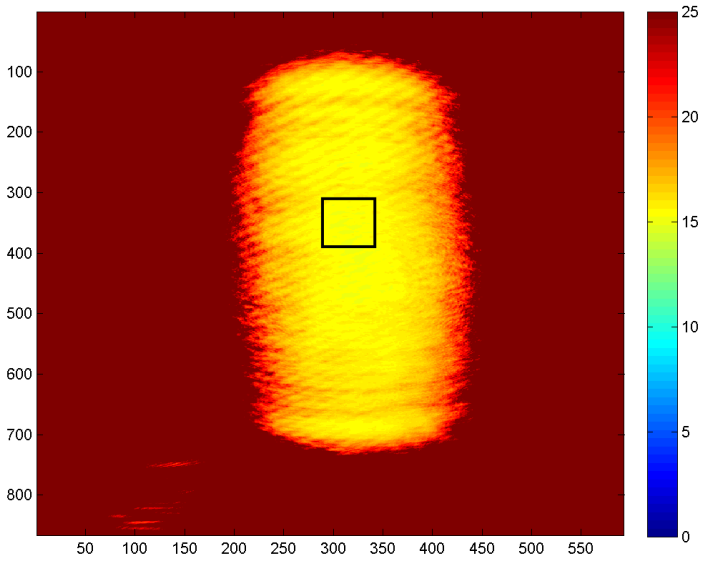

Figure 6.3: The spatial angular measurement profile of the light beam after passing through a cuvette of Maltodextrin. The black box is the region of interest from which the final angular value will be taken.

the sugar strand was incident on the photosensitive area, there would be a larger error in the estimated angle for the concentration of Maltodextrin in the solution. In Table 6.1, there is a small relative error in the estimated angle relative to the theoretical which, as we see in Table 6.2, results in only a small relative error between the actual and estimated concentrations.

Over all, we can conclude that in scenarios where the optical activity of the chiral molecules is near that of Maltordextrin DE 16.5-19.5, then the inexpensive, compact polarimeter that is designed and implemented in this thesis is capable of measuring the concentrations of those solutions with roughly 1% relative error.

Chapter 7

Conclusion

In this thesis, a novel inexpensive, compact integrated computational measurement system for enhancing polarimetric measurements for concentration estimation in chiral molecule solutions has been proposed, designed, built and implemented. This thesis also proposed and demonstrated the novel use of spatial algorithms as alternatives to the state-of-the-art Temporal Averaging for computational measurement enhancement.

The polarimeter has a very small footprint in comparison to lab-quality polarimeters for chiral concentration identification and with the use of commercial-grade elements, is relatively inexpensive. Unfortunately, due to the quality of these optical elements, error is incurred on the system. With the use of a computational algorithm and *a priori* knowledge of the system, the error can be reduced; however, there still exists noise from photon statistics and electronics which were before suppressed using Temporal Averaging of a single photosensitve area. This thesis has demonstrated that spatial detector array pixels can mimic temporal measurements and can be enhanced in a similar way to produce enhanced results. In addition, through the use of a spatial detector array, the full spot size of the light beam incident on the detector is taken advantage of and produced comparable results to Temporal Averaging.

Future Work and Applications

This thesis has demonstrated that spatial algorithms can be used to similar effect in measurement enhancement and concentration determination, relative to the state-of-the-art. In addition, it has demonstrated that polarimetric devices can be built that occupy a small footprint and be relatively inexpensive.

The spatial enhancement methods demonstrated in this thesis are rudimentary. More complex and robust spatial algorithms can be utilised to enhance polarimetric measurements in more complex scenarios, for example, when the assumption of uniform scattering across the light beam does not hold, or when low-light conditions exist and the shot noise is dominant. These are common in biological applications, like in endoscopic polarimetric analysis [32]. The use of a spatial detector array also allows for single exposure measurement enhancement. This opens the modality for use in dynamic scenarios where the motion cannot be controlled. For example, taking polarimetric measurements of the eye for glucose concentration estimation [9]. The constant motion of the eye can change the bulk properties of the tissue being analysed making Time Averaging difficult. With the use of a spatial detector, a minimal number of acquisitions can be taken to provide an accurate measurement, thereby reducing any error caused by the eye's movement.

The small footprint and cost of this device allows it to be moved outside the lab and into less constrained environments. For example, this device can be used for water bacteria analysis by measuring the phase change as it travels through a sample taken from a stream or lake [2].

APPENDICES

Appendix A

Gaussian Approximation for Poisson Distribution

In Chapter 4, enhancement methods for polarimetric measurements that utilise the full laser spot incident of a spatial detector array were formulated. These enhancement methods suppress noise from physical and electrical sources, i.e., shot noise and dark noise. The shot noise is modelled as a Poisson distribution and the dark noise is modelled as a Gaussian distribution.

We claimed in the Section 4.3 that the Poisson distribution can be approximated to a Gaussian when a powerful enough is used, i.e., when there is a large flux of photons. This Appendix Chapter will support that claim by formulating the approximation. This formulation is summarised from the work of Peacock [33].

A.1 Poisson Distribution

The Poisson distribution is a model of the probability of an event occurring given its' rate of occurrence. The distribution is formulated as

$$\mathcal{P}_\lambda(n) = \frac{\lambda^n e^{-\lambda}}{n!} \tag{A.1}$$

where λ is the rate of occurrence of an event during a unit of time and n is a number of events in that unit of time. In the case of polarimetric measurements, λ is the incoming

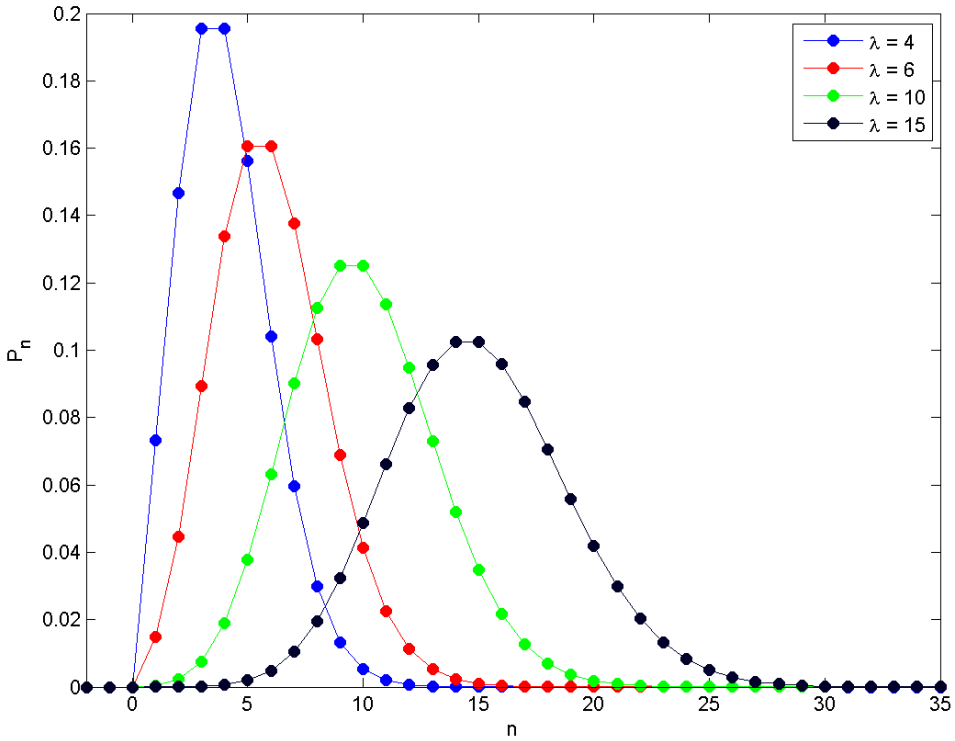

Figure A.1: A plot of the Poisson distribution for $\lambda = 4, 7, 10, 15$.

flux of photons onto the detector and n is the number of photons that will actually be incident on the detector. This implies that the objective of measurement enhancement is to recover the true flux of photons from the incident measurements on the detector. An example of the Poisson distribution for several photon arrival rates is shown in Figure A.1 and visually we can see that as λ increases, the distribution tends to a more bell-like shape. This motivates the mathematical formulation to approximate the Poisson distribution to a Gaussian distribution as λ becomes large.

A.2 Gaussian Approximation

We start the derivation of our Gaussian approximation with three other approximations. First, we provide an approximation for n

$$n = \lambda(1+\delta) \tag{A.2}$$

where $\lambda \gg 1$ and $\delta \ll 1$. We can apply this approximation for large rate of events since $\langle n \rangle = \lambda$. By the way of this approximation, we are assuming that we are only predicating the probability of an equally large number of arrivals.

This allows us to use a second approximation called the Stirling approximation where

$$n! = \sqrt{2\pi n} e^{-n} n^n \qquad \text{as} \qquad n \to \infty \tag{A.3}$$

Using the two approximations above in eq. A.1, we arrive at

$$\mathcal{P}_\lambda(n) = \frac{e^{\lambda\delta}(1+\delta)^{-\lambda(1+\delta)-1/2}}{\sqrt{2\pi\lambda}} \tag{A.4}$$

To manipulate this equation into the form of a Gaussian distribution, we need to take another approximation: the second order Taylor approximation of $\ln\left[(1+\delta)^{\lambda(1+\delta)+1/2}\right]$

$$\ln\left[(1+\delta)^{\lambda(1+\delta)+1/2}\right] = \left[\lambda(1+\delta)+1/2\right]\ln(1+\delta) = \left(\lambda(1+\delta)+1/2\right)\left(\delta + \delta^2/2 + \mathcal{O}(\delta^3)\right) \tag{A.5}$$

Using an assumption from the first approximation, $\delta \ll 1$, the Taylor approximation can reduce to

$$\ln\left[(1+\delta)^{\lambda(1+\delta)+1/2}\right] = \ldots \approx \lambda\delta + \lambda\delta^2/2 + \mathcal{O}(\delta^3) \tag{A.6}$$

We arrange eq. A.2 to solve for δ and substitute that it into eq. A.6, with $n \gg 1$, to use in eq. A.4

$$\delta = \frac{n-\lambda}{\lambda} \tag{A.7}$$

which simplifies to

$$\mathcal{P}_\lambda(n) \approx \frac{1}{\sqrt{2\pi\lambda}} e^{-\frac{(n-\lambda)^2}{2\lambda}} \tag{A.8}$$

This formulation demonstrates that as the rate of photon arrival, λ, becomes large, the Poisson distribution can be approximated to a Gaussian distribution, with mean and variance λ.

■

Appendix B

Synthetic Experiment Results

Table B.1: PSNR and angular error of measurement enhancement algorithms when contaminated with 3 e^- of dark noise and laser power 0.2500.

		PSNR(dB)				$\lvert\Delta\theta^\circ\rvert$			
Algorithm	Angle	0	5	10	15	0	5	10	15
Control		80.7830	80.7532	80.7627	80.7744	0.6958	0.1487	0.0336	0.0390
Temporal Averaging		103.3155	103.3141	103.3108	103.3182	0.2381	0.0106	0.0055	0.0063
Spatial Averaging		89.8304	89.9310	90.1038	90.1674	0.9407	0.1240	0.0711	0.0086
Model Fitting		123.0166	120.0099	130.9888	128.3047	0.1105	0.0001	0.0004	0.0001

Table B.2: Concentration estimation error of measurement enhancement algorithms when contaminated with 3 e^- of dark noise and laser power 0.2500.

		Glucose $\lvert\Delta c\rvert \frac{\text{g}}{\text{ml}}$				Maltodextrin $\lvert\Delta c\rvert \frac{\text{g}}{\text{ml}}$			
Algorithm	Angle	0	5	10	15	0	5	10	15
Control		0.1320	0.0282	0.0064	0.0074	0.0382	0.0082	0.0018	0.0021
Temporal Averaging		0.0452	0.0020	0.0010	0.0012	0.0131	0.0006	0.0003	0.0003
Spatial Averaging		0.1785	0.0235	0.0135	0.0016	0.0517	0.0068	0.0039	0.0005
Model Fitting		0.0210	0.0000	0.0001	0.0000	0.0061	0.0000	0.0000	0.0000

Table B.3: PSNR and angular error of measurement enhancement algorithms when contaminated with 3 e^- of dark noise and laser power 0.5000.

		PSNR(dB)				$\lvert\Delta\theta^\circ\rvert$			
Algorithm	Angle	0	5	10	15	0	5	10	15
Control		80.7604	80.7800	80.7671	80.7693	0.1846	0.0191	0.0144	0.0306
Temporal Averaging		103.3139	103.3121	103.3164	103.3140	0.2218	0.0083	0.0018	0.0026
Spatial Averaging		89.3140	89.3889	89.8179	89.2403	0.4274	0.0485	0.0292	0.0061
Model Fitting		148.6031	121.2190	142.7351	130.3055	0.0086	0.0006	0.0000	0.0002

Table B.4: Concentration estimation error of measurement enhancement algorithms when contaminated with 3 e^- of dark noise and laser power 0.5000.

		Glucose $\lvert\Delta c\rvert \frac{\text{g}}{\text{ml}}$				Maltodextrin $\lvert\Delta c\rvert \frac{\text{g}}{\text{ml}}$			
Algorithm	Angle	0	5	10	15	0	5	10	15
Control		0.0350	0.0036	0.0027	0.0058	0.0101	0.0011	0.0008	0.0017
Temporal Averaging		0.0421	0.0016	0.0003	0.0005	0.0122	0.0005	0.0001	0.0001
Spatial Averaging		0.0811	0.0092	0.0055	0.0012	0.0235	0.0027	0.0016	0.0003
Model Fitting		0.0016	0.0001	0.0000	0.0000	0.0005	0.0000	0.0000	0.0000

Table B.5: PSNR and angular error of measurement enhancement algorithms when contaminated with 3 e^- of dark noise and laser power 0.7500.

		PSNR(dB)				$\lvert\Delta\theta^\circ\rvert$			
Algorithm	Angle	0	5	10	15	0	5	10	15
Control		80.7769	80.7575	80.7566	80.7780	0.3035	0.0185	0.0532	0.0166
Temporal Averaging		103.3121	103.3171	103.3158	103.3149	0.1552	0.0012	0.0010	0.0026
Spatial Averaging		88.0300	87.6718	88.4760	88.7323	0.6609	0.0197	0.0124	0.0091
Model Fitting		149.5135	141.1722	126.3063	130.3758	0.0192	0.0001	0.0001	0.0001

Table B.6: Concentration estimation error of measurement enhancement algorithms when contaminated with 3 e^- of dark noise and laser power 0.7500.

		Glucose $\lvert\Delta c\rvert \frac{\text{g}}{\text{ml}}$				Maltodextrin $\lvert\Delta c\rvert \frac{\text{g}}{\text{ml}}$			
Algorithm	Angle	0	5	10	15	0	5	10	15
Control		0.0576	0.0035	0.0101	0.0032	0.0167	0.0010	0.0029	0.0009
Temporal Averaging		0.0295	0.0002	0.0002	0.0005	0.0085	0.0001	0.0001	0.0001
Spatial Averaging		0.1254	0.0037	0.0024	0.0017	0.0363	0.0011	0.0007	0.0005
Model Fitting		0.0036	0.0000	0.0000	0.0000	0.0011	0.0000	0.0000	0.0000

Table B.7: PSNR and angular error of measurement enhancement algorithms when contaminated with 3 e^- of dark noise and laser power 1.0000.

		PSNR(dB)				$\lvert\Delta\theta^\circ\rvert$			
Algorithm	Angle	0	5	10	15	0	5	10	15
Control		80.7678	80.7659	80.7676	80.7610	0.5614	0.0027	0.0336	0.0355
Temporal Averaging		103.3121	103.3168	103.3187	103.3159	0.2135	0.0018	0.0018	0.0011
Spatial Averaging		87.4373	87.4821	87.5755	87.2038	0.4905	0.0148	0.0139	0.0112
Model Fitting		136.9599	139.4726	131.5431	130.0370	0.0305	0.0001	0.0000	0.0001

Table B.8: Concentration estimation error of measurement enhancement algorithms when contaminated with 3 e^- of dark noise and laser power 1.0000.

		Glucose $\lvert\Delta c\rvert \frac{\text{g}}{\text{ml}}$				Maltodextrin $\lvert\Delta c\rvert \frac{\text{g}}{\text{ml}}$			
Algorithm	Angle	0	5	10	15	0	5	10	15
Control		0.1065	0.0005	0.0064	0.0067	0.0309	0.0001	0.0018	0.0019
Temporal Averaging		0.0405	0.0003	0.0003	0.0002	0.0117	0.0001	0.0001	0.0001
Spatial Averaging		0.0931	0.0028	0.0026	0.0021	0.0270	0.0008	0.0008	0.0006
Model Fitting		0.0058	0.0000	0.0000	0.0000	0.0017	0.0000	0.0000	0.0000

Table B.9: PSNR and angular error of measurement enhancement algorithms when contaminated with 6 e^- of dark noise and laser power 0.2500.

		PSNR(dB)				$\lvert\Delta\theta^\circ\rvert$			
Algorithm	Angle	0	5	10	15	0	5	10	15
Control		74.7584	74.7412	74.7520	74.7381	2.6671	0.5278	0.1820	0.1480
Temporal Averaging		102.8790	102.8807	102.8777	102.8744	0.3561	0.0182	0.0040	0.0088
Spatial Averaging		84.3349	84.0696	84.4126	84.0067	0.5080	0.1680	0.0055	0.0302
Model Fitting		121.0362	119.9429	121.2823	125.5051	0.1554	0.0023	0.0000	0.0001

Table B.10: Concentration estimation error of measurement enhancement algorithms when contaminated with 6 e^- of dark noise and laser power 0.2500.

		Glucose $\lvert\Delta c\rvert \frac{\text{g}}{\text{ml}}$				Maltodextrin $\lvert\Delta c\rvert \frac{\text{g}}{\text{ml}}$			
Algorithm	Angle	0	5	10	15	0	5	10	15
Control		0.5061	0.1001	0.0345	0.0281	0.1466	0.0290	0.0100	0.0081
Temporal Averaging		0.0676	0.0034	0.0008	0.0017	0.0196	0.0010	0.0002	0.0005
Spatial Averaging		0.0964	0.0319	0.0010	0.0057	0.0279	0.0092	0.0003	0.0017
Model Fitting		0.0295	0.0004	0.0000	0.0000	0.0085	0.0001	0.0000	0.0000

Table B.11: PSNR and angular error of measurement enhancement algorithms when contaminated with 6 e^- of dark noise and laser power 0.5000.

		PSNR(dB)				$\lvert\Delta\theta^\circ\rvert$			
Algorithm	Angle	0	5	10	15	0	5	10	15
Control		74.7431	74.7525	74.7361	74.7429	0.6815	0.1194	0.1266	0.0135
Temporal Averaging		102.8825	102.8823	102.8759	102.8749	0.3006	0.0036	0.0046	0.0019
Spatial Averaging		84.0137	84.0897	83.9168	84.1860	0.3623	0.1058	0.0300	0.0495
Model Fitting		133.8201	128.4372	116.7954	129.5685	0.0546	0.0002	0.0004	0.0000

Table B.12: Concentration estimation error of measurement enhancement algorithms when contaminated with 6 e^- of dark noise and laser power 0.5000.

		Glucose $\lvert\Delta c\rvert \frac{\text{g}}{\text{ml}}$				Maltodextrin $\lvert\Delta c\rvert \frac{\text{g}}{\text{ml}}$			
Algorithm	Angle	0	5	10	15	0	5	10	15
Control		0.1293	0.0227	0.0240	0.0026	0.0375	0.0066	0.0070	0.0007
Temporal Averaging		0.0570	0.0007	0.0009	0.0004	0.0165	0.0002	0.0003	0.0001
Spatial Averaging		0.0688	0.0201	0.0057	0.0094	0.0199	0.0058	0.0016	0.0027
Model Fitting		0.0104	0.0000	0.0001	0.0000	0.0030	0.0000	0.0000	0.0000

Table B.13: PSNR and angular error of measurement enhancement algorithms when contaminated with 6 e^- of dark noise and laser power 0.7500.

		PSNR(dB)				$\lvert\Delta\theta^\circ\rvert$			
Algorithm	Angle	0	5	10	15	0	5	10	15
Control		74.7565	74.7510	74.7553	74.7320	1.4250	0.1974	0.0845	0.0867
Temporal Averaging		102.8817	102.8790	102.8792	102.8731	0.1599	0.0073	0.0025	0.0015
Spatial Averaging		84.0346	83.5518	83.6305	83.6034	0.3554	0.0076	0.0212	0.0329
Model Fitting		137.1395	124.6424	134.8477	124.3177	0.0304	0.0006	0.0001	0.0002

Table B.14: Concentration estimation error of measurement enhancement algorithms when contaminated with 6 e^- of dark noise and laser power 0.7500.

		Glucose $\lvert\Delta c\rvert \frac{g}{ml}$				Maltodextrin $\lvert\Delta c\rvert \frac{g}{ml}$			
Algorithm	Angle	0	5	10	15	0	5	10	15
Control		0.2704	0.0375	0.0160	0.0165	0.0783	0.0108	0.0046	0.0048
Temporal Averaging		0.0303	0.0014	0.0005	0.0003	0.0088	0.0004	0.0001	0.0001
Spatial Averaging		0.0674	0.0014	0.0040	0.0062	0.0195	0.0004	0.0012	0.0018
Model Fitting		0.0058	0.0001	0.0000	0.0000	0.0017	0.0000	0.0000	0.0000

Table B.15: PSNR and angular error of measurement enhancement algorithms when contaminated with 6 e^- of dark noise and laser power 1.0000.

		PSNR(dB)				$\lvert\Delta\theta^\circ\rvert$			
Algorithm	Angle	0	5	10	15	0	5	10	15
Control		74.7304	74.7516	74.7337	74.7545	0.7890	0.1600	0.0316	0.0098
Temporal Averaging		102.8787	102.8723	102.8792	102.8754	0.2125	0.0036	0.0011	0.0013
Spatial Averaging		83.3405	83.2078	83.0549	83.4951	0.3886	0.0039	0.0042	0.0066
Model Fitting		139.5540	121.2346	119.6496	118.3106	0.0252	0.0002	0.0001	0.0000

Table B.16: Concentration estimation error of measurement enhancement algorithms when contaminated with 6 e^- of dark noise and laser power 1.0000.

		Glucose $\lvert\Delta c\rvert \frac{\text{g}}{\text{ml}}$				Maltodextrin $\lvert\Delta c\rvert \frac{\text{g}}{\text{ml}}$			
Algorithm	Angle	0	5	10	15	0	5	10	15
Control		0.1497	0.0304	0.0060	0.0019	0.0434	0.0088	0.0017	0.0005
Temporal Averaging		0.0403	0.0007	0.0002	0.0002	0.0117	0.0002	0.0001	0.0001
Spatial Averaging		0.0737	0.0007	0.0008	0.0013	0.0214	0.0002	0.0002	0.0004
Model Fitting		0.0048	0.0000	0.0000	0.0000	0.0014	0.0000	0.0000	0.0000

Table B.17: PSNR and angular error of measurement enhancement algorithms when contaminated with 9 e^- of dark noise and laser power 0.2500.

		PSNR(dB)				$\lvert\Delta\theta^\circ\rvert$			
Algorithm	Angle	0	5	10	15	0	5	10	15
Control		71.2272	71.2211	71.2332	71.2230	1.3919	1.2920	0.1070	0.1079
Temporal Averaging		102.6953	102.6942	102.6881	102.6957	0.3680	0.0178	0.0092	0.0076
Spatial Averaging		80.8437	80.7153	80.8914	80.4354	0.9570	0.0149	0.0404	0.0524
Model Fitting		115.7145	125.3334	117.1241	126.1459	0.1155	0.0017	0.0011	0.0007

Table B.18: Concentration estimation error of measurement enhancement algorithms when contaminated with 9 e^- of dark noise and laser power 0.2500.

		Glucose $\lvert\Delta c\rvert \frac{\text{g}}{\text{ml}}$				Maltodextrin $\lvert\Delta c\rvert \frac{\text{g}}{\text{ml}}$			
Algorithm	Angle	0	5	10	15	0	5	10	15
Control		0.2641	0.2452	0.0203	0.0205	0.0765	0.0710	0.0059	0.0059
Temporal Averaging		0.0698	0.0034	0.0018	0.0014	0.0202	0.0010	0.0005	0.0004
Spatial Averaging		0.1816	0.0028	0.0077	0.0099	0.0526	0.0008	0.0022	0.0029
Model Fitting		0.0219	0.0003	0.0002	0.0001	0.0063	0.0001	0.0001	0.0000

Table B.19: PSNR and angular error of measurement enhancement algorithms when contaminated with 9 e^- of dark noise and laser power 0.5000.

		PSNR(dB)				$\lvert\Delta\theta^\circ\rvert$			
Algorithm	Angle	0	5	10	15	0	5	10	15
Control		71.2239	71.2184	71.2233	71.1973	1.8722	0.0792	0.0636	0.0048
Temporal Averaging		102.6875	102.6863	102.6912	102.6875	0.2341	0.0073	0.0037	0.0033
Spatial Averaging		80.6151	80.3995	80.6672	80.7483	1.0538	0.0818	0.0378	0.0034
Model Fitting		112.7323	116.8873	114.8749	117.8677	0.1115	0.0007	0.0002	0.0001

Table B.20: Concentration estimation error of measurement enhancement algorithms when contaminated with 9 e^- of dark noise and laser power 0.5000.

		Glucose $\lvert\Delta c\rvert \frac{\text{g}}{\text{ml}}$				Maltodextrin $\lvert\Delta c\rvert \frac{\text{g}}{\text{ml}}$			
Algorithm	Angle	0	5	10	15	0	5	10	15
Control		0.3553	0.0150	0.0121	0.0009	0.1029	0.0044	0.0035	0.0003
Temporal Averaging		0.0444	0.0014	0.0007	0.0006	0.0129	0.0004	0.0002	0.0002
Spatial Averaging		0.2000	0.0155	0.0072	0.0007	0.0579	0.0045	0.0021	0.0002
Model Fitting		0.0212	0.0001	0.0000	0.0000	0.0061	0.0000	0.0000	0.0000

Table B.21: PSNR and angular error of measurement enhancement algorithms when contaminated with 9 e^- of dark noise and laser power 0.7500.

		PSNR(dB)				$\lvert\Delta\theta^\circ\rvert$			
Algorithm	Angle	0	5	10	15	0	5	10	15
Control		71.2198	71.2287	71.2247	71.2253	0.9701	0.1435	0.0031	0.0572
Temporal Averaging		102.6929	102.6898	102.6898	102.6919	0.2233	0.0036	0.0036	0.0017
Spatial Averaging		80.3812	80.5570	80.5884	80.3936	0.7035	0.0177	0.0126	0.0021
Model Fitting		120.4456	107.3458	118.2449	122.0444	0.1106	0.0012	0.0000	0.0003

Table B.22: Concentration estimation error of measurement enhancement algorithms when contaminated with 9 e^- of dark noise and laser power 0.7500.

		Glucose $\lvert\Delta c\rvert \frac{\text{g}}{\text{ml}}$				Maltodextrin $\lvert\Delta c\rvert \frac{\text{g}}{\text{ml}}$			
Algorithm	Angle	0	5	10	15	0	5	10	15
Control		0.1841	0.0272	0.0006	0.0109	0.0533	0.0079	0.0002	0.0031
Temporal Averaging		0.0424	0.0007	0.0007	0.0003	0.0123	0.0002	0.0002	0.0001
Spatial Averaging		0.1335	0.0034	0.0024	0.0004	0.0387	0.0010	0.0007	0.0001
Model Fitting		0.0210	0.0002	0.0000	0.0001	0.0061	0.0001	0.0000	0.0000

Table B.23: PSNR and angular error of measurement enhancement algorithms when contaminated with 9 e^- of dark noise and laser power 1.0000.

		PSNR(dB)				$\lvert\Delta\theta^\circ\rvert$			
Algorithm	Angle	0	5	10	15	0	5	10	15
Control		71.2208	71.2287	71.2291	71.2196	0.7523	0.0777	0.0432	0.0176
Temporal Averaging		102.6922	102.6932	102.6845	102.6901	0.2125	0.0045	0.0028	0.0007
Spatial Averaging		80.3465	80.4745	79.9432	80.4329	0.8985	0.0324	0.0160	0.0208
Model Fitting		117.6393	137.5968	121.6387	122.2505	0.0043	0.0001	0.0005	0.0001

Table B.24: Concentration estimation error of measurement enhancement algorithms when contaminated with 9 e^- of dark noise and laser power 1.0000.

		Glucose $\lvert\Delta c\rvert \frac{\text{g}}{\text{ml}}$				Maltodextrin $\lvert\Delta c\rvert \frac{\text{g}}{\text{ml}}$			
Algorithm	Angle	0	5	10	15	0	5	10	15
Control		0.1427	0.0147	0.0082	0.0033	0.0413	0.0043	0.0024	0.0010
Temporal Averaging		0.0403	0.0009	0.0005	0.0001	0.0117	0.0002	0.0002	0.0000
Spatial Averaging		0.1705	0.0062	0.0030	0.0039	0.0494	0.0018	0.0009	0.0011
Model Fitting		0.0008	0.0000	0.0001	0.0000	0.0002	0.0000	0.0000	0.0000

Table B.25: PSNR and angular error of measurement enhancement algorithms when contaminated with 12 e^- of dark noise and laser power 0.2500.

		PSNR(dB)				$\lvert\Delta\theta^\circ\rvert$			
Algorithm	Angle	0	5	10	15	0	5	10	15
Control		68.7364	68.7196	68.7407	68.7310	0.9643	0.7776	0.6071	0.0682
Temporal Averaging		102.5783	102.5718	102.5741	102.5790	0.4419	0.0125	0.0080	0.0063
Spatial Averaging		77.9575	78.2046	78.2631	78.5254	0.8532	0.2165	0.0167	0.0877
Model Fitting		113.0555	106.0586	109.3179	122.8290	0.1605	0.0026	0.0001	0.0008

Table B.26: Concentration estimation error of measurement enhancement algorithms when contaminated with 12 e^- of dark noise and laser power 0.2500.

		Glucose $\lvert\Delta c\rvert \frac{\text{g}}{\text{ml}}$				Maltodextrin $\lvert\Delta c\rvert \frac{\text{g}}{\text{ml}}$			
Algorithm	Angle	0	5	10	15	0	5	10	15
Control		0.1830	0.1476	0.1152	0.0129	0.0530	0.0427	0.0334	0.0037
Temporal Averaging		0.0839	0.0024	0.0015	0.0012	0.0243	0.0007	0.0004	0.0003
Spatial Averaging		0.1619	0.0411	0.0032	0.0166	0.0469	0.0119	0.0009	0.0048
Model Fitting		0.0305	0.0005	0.0000	0.0002	0.0088	0.0001	0.0000	0.0000

Table B.27: PSNR and angular error of measurement enhancement algorithms when contaminated with 12 e^- of dark noise and laser power 0.5000.

		PSNR(dB)				$\lvert\Delta\theta^\circ\rvert$			
Algorithm	Angle	0	5	10	15	0	5	10	15
Control		68.7282	68.7273	68.7203	68.7342	0.5059	0.3959	0.1190	0.1555
Temporal Averaging		102.5838	102.5783	102.5783	102.5740	0.3292	0.0103	0.0037	0.0025
Spatial Averaging		78.4226	78.1807	78.4273	77.7211	0.4933	0.0726	0.1688	0.1047
Model Fitting		109.2873	123.2233	119.5449	130.3748	0.1442	0.0007	0.0011	0.0002

Table B.28: Concentration estimation error of measurement enhancement algorithms when contaminated with 12 e^- of dark noise and laser power 0.5000.

		Glucose $\lvert\Delta c\rvert \frac{\text{g}}{\text{ml}}$				Maltodextrin $\lvert\Delta c\rvert \frac{\text{g}}{\text{ml}}$			
Algorithm	Angle	0	5	10	15	0	5	10	15
Control		0.0960	0.0751	0.0226	0.0295	0.0278	0.0218	0.0065	0.0085
Temporal Averaging		0.0625	0.0020	0.0007	0.0005	0.0181	0.0006	0.0002	0.0001
Spatial Averaging		0.0936	0.0138	0.0320	0.0199	0.0271	0.0040	0.0093	0.0058
Model Fitting		0.0274	0.0001	0.0002	0.0000	0.0079	0.0000	0.0001	0.0000

Table B.29: PSNR and angular error of measurement enhancement algorithms when contaminated with 12 e^- of dark noise and laser power 0.7500.

		PSNR(dB)				$\lvert\Delta\theta^\circ\rvert$			
Algorithm	Angle	0	5	10	15	0	5	10	15
Control		68.7192	68.7206	68.7172	68.7171	1.5661	0.1511	0.1451	0.0445
Temporal Averaging		102.5775	102.5766	102.5735	102.5828	0.1901	0.0084	0.0037	0.0017
Spatial Averaging		78.2360	77.8875	78.0139	78.3761	0.3214	0.0437	0.0683	0.0144
Model Fitting		123.1782	127.5087	118.2382	133.5582	0.1026	0.0001	0.0000	0.0000

Table B.30: Concentration estimation error of measurement enhancement algorithms when contaminated with 12 e^- of dark noise and laser power 0.7500.

		Glucose $\lvert\Delta c\rvert \frac{\text{g}}{\text{ml}}$				Maltodextrin $\lvert\Delta c\rvert \frac{\text{g}}{\text{ml}}$			
Algorithm	Angle	0	5	10	15	0	5	10	15
Control		0.2972	0.0287	0.0275	0.0085	0.0861	0.0083	0.0080	0.0024
Temporal Averaging		0.0361	0.0016	0.0007	0.0003	0.0104	0.0005	0.0002	0.0001
Spatial Averaging		0.0610	0.0083	0.0130	0.0027	0.0177	0.0024	0.0038	0.0008
Model Fitting		0.0195	0.0000	0.0000	0.0000	0.0056	0.0000	0.0000	0.0000

Table B.31: PSNR and angular error of measurement enhancement algorithms when contaminated with 12 e^- of dark noise and laser power 1.0000.

		PSNR(dB)				$\lvert\Delta\theta^\circ\rvert$			
Algorithm	Angle	0	5	10	15	0	5	10	15
Control		68.7362	68.7364	68.7272	68.7179	0.3822	0.0431	0.0291	0.0303
Temporal Averaging		102.5815	102.5830	102.5788	102.5893	0.2125	0.0027	0.0025	0.0009
Spatial Averaging		77.8060	77.5428	77.9445	77.6520	0.8942	0.0683	0.0185	0.0079
Model Fitting		109.3138	113.9898	109.6298	120.5780	0.0166	0.0011	0.0001	0.0001

Table B.32: Concentration estimation error of measurement enhancement algorithms when contaminated with 12 e^- of dark noise and laser power 1.0000.

		Glucose $\lvert\Delta c\rvert \frac{\text{g}}{\text{ml}}$				Maltodextrin $\lvert\Delta c\rvert \frac{\text{g}}{\text{ml}}$			
Algorithm	Angle	0	5	10	15	0	5	10	15
Control		0.0725	0.0082	0.0055	0.0058	0.0210	0.0024	0.0016	0.0017
Temporal Averaging		0.0403	0.0005	0.0005	0.0002	0.0117	0.0001	0.0001	0.0001
Spatial Averaging		0.1697	0.0130	0.0035	0.0015	0.0491	0.0038	0.0010	0.0004
Model Fitting		0.0031	0.0002	0.0000	0.0000	0.0009	0.0001	0.0000	0.0000

Table B.33: PSNR and angular error of measurement enhancement algorithms when contaminated with 15 e^- of dark noise and laser power 0.2500.

		PSNR(dB)				$\lvert\Delta\theta^\circ\rvert$			
Algorithm	Angle	0	5	10	15	0	5	10	15
Control		66.7799	66.7962	66.7813	66.7832	2.2627	0.6099	0.3640	0.2419
Temporal Averaging		102.4991	102.5079	102.5022	102.5067	0.5029	0.0217	0.0111	0.0038
Spatial Averaging		76.1910	76.1858	76.0264	76.3019	1.6415	0.1655	0.2391	0.0222
Model Fitting		117.8009	109.2136	127.8316	113.2092	0.1892	0.0028	0.0006	0.0006

Table B.34: Concentration estimation error of measurement enhancement algorithms when contaminated with 15 e^- of dark noise and laser power 0.2500.

		Glucose $\lvert\Delta c\rvert \frac{g}{ml}$				Maltodextrin $\lvert\Delta c\rvert \frac{g}{ml}$			
Algorithm	Angle	0	5	10	15	0	5	10	15
Control		0.4294	0.1157	0.0691	0.0459	0.1243	0.0335	0.0200	0.0133
Temporal Averaging		0.0954	0.0041	0.0021	0.0007	0.0276	0.0012	0.0006	0.0002
Spatial Averaging		0.3115	0.0314	0.0454	0.0042	0.0902	0.0091	0.0131	0.0012
Model Fitting		0.0359	0.0005	0.0001	0.0001	0.0104	0.0002	0.0000	0.0000

Table B.35: PSNR and angular error of measurement enhancement algorithms when contaminated with 15 e^- of dark noise and laser power 0.5000.

		PSNR(dB)				$\lvert\Delta\theta^\circ\rvert$			
Algorithm	Angle	0	5	10	15	0	5	10	15
Control		66.7885	66.7924	66.7775	66.7952	2.8887	0.2040	0.3316	0.0193
Temporal Averaging		102.5065	102.5052	102.5039	102.5003	0.2917	0.0127	0.0041	0.0025
Spatial Averaging		76.5805	76.3844	76.4191	76.1480	0.1488	0.0023	0.0691	0.0550
Model Fitting		112.0326	121.4583	117.3324	108.5959	0.0486	0.0015	0.0014	0.0005

Table B.36: Concentration estimation error of measurement enhancement algorithms when contaminated with 15 e^- of dark noise and laser power 0.5000.

		Glucose $\lvert\Delta c\rvert \frac{g}{ml}$				Maltodextrin $\lvert\Delta c\rvert \frac{g}{ml}$			
Algorithm	Angle	0	5	10	15	0	5	10	15
Control		0.5481	0.0387	0.0629	0.0037	0.1587	0.0112	0.0182	0.0011
Temporal Averaging		0.0553	0.0024	0.0008	0.0005	0.0160	0.0007	0.0002	0.0001
Spatial Averaging		0.0282	0.0004	0.0131	0.0104	0.0082	0.0001	0.0038	0.0030
Model Fitting		0.0092	0.0003	0.0003	0.0001	0.0027	0.0001	0.0001	0.0000

Table B.37: PSNR and angular error of measurement enhancement algorithms when contaminated with 15 e^- of dark noise and laser power 0.7500.

		PSNR(dB)				$\lvert\Delta\theta^\circ\rvert$			
Algorithm	Angle	0	5	10	15	0	5	10	15
Control		66.7946	66.7881	66.7867	66.7808	1.2016	0.2799	0.1547	0.1210
Temporal Averaging		102.5041	102.5032	102.4999	102.5089	0.2195	0.0052	0.0006	0.0016
Spatial Averaging		76.2999	76.4213	75.9003	76.2927	0.2273	0.2793	0.1050	0.0049
Model Fitting		114.8423	112.4828	127.1538	117.1788	0.0398	0.0011	0.0001	0.0005

Table B.38: Concentration estimation error of measurement enhancement algorithms when contaminated with 15 e^- of dark noise and laser power 0.7500.

		Glucose $\lvert\Delta c\rvert \frac{\text{g}}{\text{ml}}$				Maltodextrin $\lvert\Delta c\rvert \frac{\text{g}}{\text{ml}}$			
Algorithm	Angle	0	5	10	15	0	5	10	15
Control		0.2280	0.0531	0.0294	0.0230	0.0660	0.0154	0.0085	0.0066
Temporal Averaging		0.0417	0.0010	0.0001	0.0003	0.0121	0.0003	0.0000	0.0001
Spatial Averaging		0.0431	0.0530	0.0199	0.0009	0.0125	0.0153	0.0058	0.0003
Model Fitting		0.0076	0.0002	0.0000	0.0001	0.0022	0.0001	0.0000	0.0000

Table B.39: PSNR and angular error of measurement enhancement algorithms when contaminated with 15 e^- of dark noise and laser power 1.0000.

		PSNR(dB)				$\lvert\Delta\theta^\circ\rvert$			
Algorithm	Angle	0	5	10	15	0	5	10	15
Control		66.7894	66.7918	66.7987	66.7922	1.5118	0.3241	0.4422	0.0677
Temporal Averaging		102.5080	102.5047	102.5027	102.5062	0.2688	0.0036	0.0011	0.0019
Spatial Averaging		76.0922	76.3000	76.1921	76.3930	1.1619	0.0275	0.0609	0.0488
Model Fitting		128.9984	110.1192	114.9669	132.1786	0.0374	0.0011	0.0005	0.0001

Table B.40: Concentration estimation error of measurement enhancement algorithms when contaminated with 15 e^- of dark noise and laser power 1.0000.

		Glucose $\lvert\Delta c\rvert \frac{g}{ml}$				Maltodextrin $\lvert\Delta c\rvert \frac{g}{ml}$			
Algorithm	Angle	0	5	10	15	0	5	10	15
Control		0.2869	0.0615	0.0839	0.0129	0.0831	0.0178	0.0243	0.0037
Temporal Averaging		0.0510	0.0007	0.0002	0.0004	0.0148	0.0002	0.0001	0.0001
Spatial Averaging		0.2205	0.0052	0.0116	0.0093	0.0639	0.0015	0.0033	0.0027
Model Fitting		0.0071	0.0002	0.0001	0.0000	0.0021	0.0001	0.0000	0.0000

Table B.41: PSNR and angular error of measurement enhancement algorithms when contaminated with 18 e^- of dark noise and laser power 0.2500.

		PSNR(dB)				$\lvert\Delta\theta^\circ\rvert$			
Algorithm	Angle	0	5	10	15	0	5	10	15
Control		65.2000	65.1991	65.2162	65.1992	2.2549	0.9769	0.1761	0.1651
Temporal Averaging		102.4514	102.4505	102.4448	102.4536	0.3751	0.0180	0.0077	0.0050
Spatial Averaging		74.6430	75.0879	75.0463	74.5974	2.2460	0.0527	0.1649	0.0316
Model Fitting		110.5476	124.2781	107.3791	113.3204	0.1720	0.0006	0.0005	0.0002

Table B.42: Concentration estimation error of measurement enhancement algorithms when contaminated with 18 e^- of dark noise and laser power 0.2500.

		Glucose $\lvert\Delta c\rvert \frac{\text{g}}{\text{ml}}$				Maltodextrin $\lvert\Delta c\rvert \frac{\text{g}}{\text{ml}}$			
Algorithm	Angle	0	5	10	15	0	5	10	15
Control		0.4279	0.1854	0.0334	0.0313	0.1239	0.0537	0.0097	0.0091
Temporal Averaging		0.0712	0.0034	0.0015	0.0010	0.0206	0.0010	0.0004	0.0003
Spatial Averaging		0.4262	0.0100	0.0313	0.0060	0.1234	0.0029	0.0091	0.0017
Model Fitting		0.0326	0.0001	0.0001	0.0000	0.0095	0.0000	0.0000	0.0000

Table B.43: PSNR and angular error of measurement enhancement algorithms when contaminated with 18 e^- of dark noise and laser power 0.5000.

		PSNR(dB)				$\lvert\Delta\theta^\circ\rvert$			
Algorithm	Angle	0	5	10	15	0	5	10	15
Control		65.1994	65.2095	65.2126	65.1966	2.1001	0.3746	0.1978	0.2289
Temporal Averaging		102.4399	102.4528	102.4542	102.4550	0.3207	0.0080	0.0018	0.0019
Spatial Averaging		74.9627	74.8199	74.7210	74.8154	1.4609	0.1104	0.1023	0.0060
Model Fitting		108.2998	137.2389	118.9119	126.1194	0.2428	0.0001	0.0001	0.0001

Table B.44: Concentration estimation error of measurement enhancement algorithms when contaminated with 18 e^- of dark noise and laser power 0.5000.

		Glucose $\lvert\Delta c\rvert \frac{g}{ml}$				Maltodextrin $\lvert\Delta c\rvert \frac{g}{ml}$			
Algorithm	Angle	0	5	10	15	0	5	10	15
Control		0.3985	0.0711	0.0375	0.0434	0.1154	0.0206	0.0109	0.0126
Temporal Averaging		0.0609	0.0015	0.0003	0.0004	0.0176	0.0004	0.0001	0.0001
Spatial Averaging		0.2772	0.0210	0.0194	0.0011	0.0803	0.0061	0.0056	0.0003
Model Fitting		0.0461	0.0000	0.0000	0.0000	0.0133	0.0000	0.0000	0.0000

Table B.45: PSNR and angular error of measurement enhancement algorithms when contaminated with 18 e^- of dark noise and laser power 0.7500.

		PSNR(dB)				$\lvert\Delta\theta^\circ\rvert$			
Algorithm	Angle	0	5	10	15	0	5	10	15
Control		65.2086	65.2014	65.2049	65.2061	0.5955	0.3358	0.1159	0.0415
Temporal Averaging		102.4524	102.4564	102.4424	102.4488	0.2257	0.0069	0.0041	0.0013
Spatial Averaging		74.1054	74.3703	74.6062	74.5158	0.7155	0.0843	0.0407	0.0054
Model Fitting		129.2026	128.0139	115.5440	117.0598	0.0320	0.0005	0.0002	0.0004

Table B.46: Concentration estimation error of measurement enhancement algorithms when contaminated with 18 e^- of dark noise and laser power 0.7500.

		Glucose $\lvert\Delta c\rvert \frac{\text{g}}{\text{ml}}$				Maltodextrin $\lvert\Delta c\rvert \frac{\text{g}}{\text{ml}}$			
Algorithm	Angle	0	5	10	15	0	5	10	15
Control		0.1130	0.0637	0.0220	0.0079	0.0327	0.0185	0.0064	0.0023
Temporal Averaging		0.0428	0.0013	0.0008	0.0002	0.0124	0.0004	0.0002	0.0001
Spatial Averaging		0.1358	0.0160	0.0077	0.0010	0.0393	0.0046	0.0022	0.0003
Model Fitting		0.0061	0.0001	0.0000	0.0001	0.0018	0.0000	0.0000	0.0000

Table B.47: PSNR and angular error of measurement enhancement algorithms when contaminated with 18 e^- of dark noise and laser power 1.0000.

		PSNR(dB)				$\lvert\Delta\theta^\circ\rvert$			
Algorithm	Angle	0	5	10	15	0	5	10	15
Control		65.1992	65.2012	65.1970	65.1902	2.0224	0.5103	0.0736	0.0027
Temporal Averaging		102.4493	102.4475	102.4469	102.4520	0.2083	0.0030	0.0018	0.0012
Spatial Averaging		74.6190	74.6348	74.3982	74.7543	0.8320	0.0814	0.0682	0.0614
Model Fitting		124.9795	108.5967	112.8116	119.7132	0.0794	0.0005	0.0005	0.0004

Table B.48: Concentration estimation error of measurement enhancement algorithms when contaminated with 18 e^- of dark noise and laser power 1.0000.

		Glucose $\lvert\Delta c\rvert \frac{\text{g}}{\text{ml}}$				Maltodextrin $\lvert\Delta c\rvert \frac{\text{g}}{\text{ml}}$			
Algorithm	Angle	0	5	10	15	0	5	10	15
Control		0.3838	0.0968	0.0140	0.0005	0.1111	0.0280	0.0040	0.0001
Temporal Averaging		0.0395	0.0006	0.0003	0.0002	0.0114	0.0002	0.0001	0.0001
Spatial Averaging		0.1579	0.0154	0.0129	0.0117	0.0457	0.0045	0.0037	0.0034
Model Fitting		0.0151	0.0001	0.0001	0.0001	0.0044	0.0000	0.0000	0.0000

Table B.49: PSNR and angular error of measurement enhancement algorithms when contaminated with 21 e^- of dark noise and laser power 0.2500.

		PSNR(dB)				$\lvert\Delta\theta^\circ\rvert$			
Algorithm	Angle	0	5	10	15	0	5	10	15
Control		63.8778	63.8604	63.8654	63.8592	3.3064	0.3116	0.5217	0.3726
Temporal Averaging		102.4095	102.4021	102.4086	102.4043	0.3802	0.0150	0.0019	0.0050
Spatial Averaging		73.5239	73.5705	73.3702	73.4880	1.5087	0.1208	0.3918	0.1968
Model Fitting		118.8408	116.0517	115.3539	107.3273	0.2337	0.0044	0.0016	0.0012

Table B.50: Concentration estimation error of measurement enhancement algorithms when contaminated with 21 e^- of dark noise and laser power 0.2500.

		Glucose $\lvert\Delta c\rvert \frac{\text{g}}{\text{ml}}$				Maltodextrin $\lvert\Delta c\rvert \frac{\text{g}}{\text{ml}}$			
Algorithm	Angle	0	5	10	15	0	5	10	15
Control		0.6274	0.0591	0.0990	0.0707	0.1817	0.0171	0.0287	0.0205
Temporal Averaging		0.0721	0.0028	0.0004	0.0010	0.0209	0.0008	0.0001	0.0003
Spatial Averaging		0.2863	0.0229	0.0744	0.0373	0.0829	0.0066	0.0215	0.0108
Model Fitting		0.0444	0.0008	0.0003	0.0002	0.0128	0.0002	0.0001	0.0001

Table B.51: PSNR and angular error of measurement enhancement algorithms when contaminated with 21 e^- of dark noise and laser power 0.5000.

		PSNR(dB)				$\lvert\Delta\theta^\circ\rvert$			
Algorithm	Angle	0	5	10	15	0	5	10	15
Control		63.8564	63.8618	63.8625	63.8676	3.6898	0.2021	0.1188	0.1448
Temporal Averaging		102.4113	102.4100	102.4071	102.4058	0.3292	0.0088	0.0059	0.0019
Spatial Averaging		73.1833	73.1235	73.4221	73.3288	2.2981	0.5787	0.0204	0.0180
Model Fitting		117.5103	108.1946	123.0075	107.1269	0.0649	0.0009	0.0006	0.0004

Table B.52: Concentration estimation error of measurement enhancement algorithms when contaminated with 21 e^- of dark noise and laser power 0.5000.

		Glucose $\lvert\Delta c\rvert \frac{\text{g}}{\text{ml}}$				Maltodextrin $\lvert\Delta c\rvert \frac{\text{g}}{\text{ml}}$			
Algorithm	Angle	0	5	10	15	0	5	10	15
Control		0.7002	0.0383	0.0225	0.0275	0.2028	0.0111	0.0065	0.0080
Temporal Averaging		0.0625	0.0017	0.0011	0.0004	0.0181	0.0005	0.0003	0.0001
Spatial Averaging		0.4361	0.1098	0.0039	0.0034	0.1263	0.0318	0.0011	0.0010
Model Fitting		0.0123	0.0002	0.0001	0.0001	0.0036	0.0000	0.0000	0.0000

Table B.53: PSNR and angular error of measurement enhancement algorithms when contaminated with 21 e^- of dark noise and laser power 0.7500.

		PSNR(dB)				$\lvert\Delta\theta^\circ\rvert$			
Algorithm	Angle	0	5	10	15	0	5	10	15
Control		63.8858	63.8654	63.8637	63.8639	2.5557	0.3823	0.1482	0.1085
Temporal Averaging		102.4037	102.4074	102.4073	102.4017	0.2413	0.0076	0.0031	0.0033
Spatial Averaging		73.6624	72.9766	73.3966	72.9574	1.5567	0.0626	0.0303	0.0326
Model Fitting		118.5185	112.0150	118.8741	115.5072	0.0587	0.0014	0.0002	0.0007

Table B.54: Concentration estimation error of measurement enhancement algorithms when contaminated with 21 e^- of dark noise and laser power 0.7500.

		Glucose $\lvert\Delta c\rvert \frac{\text{g}}{\text{ml}}$				Maltodextrin $\lvert\Delta c\rvert \frac{\text{g}}{\text{ml}}$			
Algorithm	Angle	0	5	10	15	0	5	10	15
Control		0.4850	0.0725	0.0281	0.0206	0.1404	0.0210	0.0081	0.0060
Temporal Averaging		0.0458	0.0014	0.0006	0.0006	0.0133	0.0004	0.0002	0.0002
Spatial Averaging		0.2954	0.0119	0.0057	0.0062	0.0855	0.0034	0.0017	0.0018
Model Fitting		0.0111	0.0003	0.0000	0.0001	0.0032	0.0001	0.0000	0.0000

Table B.55: PSNR and angular error of measurement enhancement algorithms when contaminated with 21 e^- of dark noise and laser power 1.0000.

		PSNR(dB)				$\lvert\Delta\theta^\circ\rvert$			
Algorithm	Angle	0	5	10	15	0	5	10	15
Control		63.8683	63.8580	63.8498	63.8712	0.3191	0.2937	0.1673	0.0324
Temporal Averaging		102.4095	102.4051	102.4118	102.4058	0.1901	0.0033	0.0016	0.0013
Spatial Averaging		73.3617	73.2893	73.1762	73.2837	1.4463	0.1576	0.0257	0.0210
Model Fitting		113.0969	121.4336	107.6205	111.5707	0.1251	0.0002	0.0003	0.0001

Table B.56: Concentration estimation error of measurement enhancement algorithms when contaminated with 21 e^- of dark noise and laser power 1.0000.

		Glucose $\lvert\Delta c\rvert \frac{g}{ml}$				Maltodextrin $\lvert\Delta c\rvert \frac{g}{ml}$			
Algorithm	Angle	0	5	10	15	0	5	10	15
Control		0.0606	0.0557	0.0318	0.0061	0.0175	0.0161	0.0092	0.0018
Temporal Averaging		0.0361	0.0006	0.0003	0.0002	0.0104	0.0002	0.0001	0.0001
Spatial Averaging		0.2744	0.0299	0.0049	0.0040	0.0795	0.0087	0.0014	0.0012
Model Fitting		0.0237	0.0000	0.0001	0.0000	0.0069	0.0000	0.0000	0.0000

References

[1] H. G. Tompkins, *A User's Guide to Ellipsometry*. Academic Press, 2012.

[2] V. V. Tuchin, L. Wang, and D. A. Zimnyakov, *Optical Polarization in Biomedical Applications*. Springer Science & Business Media, 2006.

[3] T. J. Tidwell, R. De Paula, M. Y. Smadi, and V. V. Keasler, "Flow cytometry as a tool for oilfield biocide efficacy testing and monitoring," *International Biodeterioration & Biodegradation*, vol. 98, pp. 26–34, 2015.

[4] S. Yermolenko, A. Ushenko, P. Ivashko, F. Goudail, I. Gruia, C. Gavrilă, D. Zimnyakov, and A. Mikhailova, "Spectropolarimetry of cancer change of biotissues," in *Correlation Optics 2009*. International Society for Optics and Photonics, 2009, pp. 73 881D–73 881D.

[5] S. B. Yermolenko, O. V. Angelsky, A. G. Ushenko, V. P. Pishak, and O. V. Pishak, "Laser polarimetry tomography of biotissue pathological changes," in *International Conference on Optoelectronic Information Technologies*. International Society for Optics and Photonics, 2001, pp. 117–123.

[6] A. Pierangelo, A. Benali, M.-R. Antonelli, T. Novikova, P. Validire, B. Gayet, and A. De Martino, "Ex-vivo characterization of human colon cancer by mueller polarimetric imaging," *Optics Express*, vol. 19, no. 2, pp. 1582–1593, 2011.

[7] O. V. Angelsky, A. G. Ushenko, D. N. Burkovets, V. P. Pishak, and O. V. Pishak, "Laser polarimetry of pathological changes in biotissues," in *Seventh International Symposium on Laser Metrology Applied to Science, Industry, and Everyday Life*. International Society for Optics and Photonics, 2002, pp. 1045–1049.

[8] R. R. Ansari, S. Bo, L. Rovati *et al.*, "New optical scheme for a polarimetric-based glucose sensor," *Journal of Biomedical Optics*, vol. 9, no. 1, pp. 103–115, 2004.

[9] V. V. Tuchin, *Handbook of Optical Sensing of Glucose in Biological Fluids and Tissues*. CRC press, 2008.

[10] C. W. Pirnstill, D. Grunden, and G. L. Coté, "Polarimetric glucose sensing in vitro: a high frequency approach," in *SPIE BiOS*. International Society for Optics and Photonics, 2013, pp. 859 101–859 101.

[11] C. Han and W. Y. Tam, "Plasmonic ultra-broadband polarizers based on Ag nano wire-slit arrays," *Applied Physics Letters*, vol. 106, no. 8, p. 081102, 2015.

[12] M. W. Jones and C. M. Persons, "Performance predictions for micro-polarizer array imaging polarimeters," in *Optical Engineering+ Applications*. International Society for Optics and Photonics, 2007, pp. 668 208–668 208.

[13] W.-L. Hsu, J. Davis, K. Balakrishnan, M. Ibn-Elhaj, S. Kroto, N. Brock, and S. Pau, "Polarization microscope using a near infrared full-stokes imaging polarimeter," *Optics Express*, vol. 23, no. 4, pp. 4357–4368, 2015.

[14] W. Guo, Z. Li, H. Gao, L. Xia, L. Shi, Q. Deng, and C. Du, "Design of infrared polarizer based on sub-wavelength metal wire grid," in *International Symposium on Precision Engineering Measurement and Instrumentation 2012*. International Society for Optics and Photonics, 2013, pp. 87 593I–87 593I.

[15] C. S. Chun, D. L. Fleming, W. Harvey, and E. Torok, "Polarization-sensitive infrared sensor for target discrimination," in *Optical Science, Engineering and Instrumentation'97*. International Society for Optics and Photonics, 1997, pp. 55–62.

[16] G. E. Healey and R. Kondepudy, "Radiometric ccd camera calibration and noise estimation," *Pattern Analysis and Machine Intelligence, IEEE Transactions on*, vol. 16, no. 3, pp. 267–276, 1994.

[17] G. Purvinis, B. D. Cameron, and D. M. Altrogge, "Noninvasive polarimetric-based glucose monitoring: an in vivo study," *Journal of Diabetes Science And Technology*, vol. 5, no. 2, pp. 380–387, 2011.

[18] D. T. Grunden, C. W. Pirnstill, and G. L. Coté, "High-speed dual-wavelength optical polarimetry for glucose sensing," in *SPIE BiOS*. International Society for Optics and Photonics, 2014, pp. 895 111–895 111.

[19] D. H. Goldstein, *Polarized Light, revised and expanded*. CRC Press, 2011, vol. 83.

[20] E. Collett, *Field Guide to Polarization*. SPIE Press, 2005, vol. 15.

[21] P. Fieguth, *Statistical Image Processing and Mutidimensional Modeling*. Springer Science & Business Media, 2010.

[22] J. B. Breckinridge and B. R. Oppenheimer, "Polarization effects in reflecting coronagraphs for white-light applications in astronomy," *The Astrophysical Journal*, vol. 600, no. 2, p. 1091, 2004.

[23] I. J. Vaughn and B. G. Hoover, "Noise reduction in a laser polarimeter based on discrete waveplate rotations," *Optics Express*, vol. 16, no. 3, pp. 2091–2108, 2008.

[24] J. S. Tyo, "Noise equalization in stokes parameter images obtained by use of variable-retardance polarimeters," *Optics Letters*, vol. 25, no. 16, pp. 1198–1200, 2000.

[25] B. Le Jeune, J.-P. Marie, P.-Y. Gerligand, J. Cariou, and J. Lotrian, "Mueller matrix formalism in imagery: an experimental arrangement for noise reduction," in *SPIE's 1994 International Symposium on Optics, Imaging, and Instrumentation*. International Society for Optics and Photonics, 1994, pp. 443–451.

[26] J. Boulanger, C. Kervrann, P. Bouthemy, P. Elbau, J. Sibarita, and J. Salamero, "Patch-based nonlocal functional for denoising fluorescence microscopy image sequences," *Medical Imaging, IEEE Transactions on*, vol. 29, pp. 442–454, 2010.

[27] F. Luisier, T. Blu, and M. Unser, "Image denoising in mixed poisson–gaussian noise," *Image Processing, IEEE Transactions on*, vol. 20, no. 3, pp. 696–708, 2011.

[28] M. Makitalo and A. Foi, "Optimal inversion of the generalized anscombe transformation for poisson-gaussian noise," *Image Processing, IEEE Transactions on*, vol. 22, no. 1, pp. 91–103, 2013.

[29] W. M. Haynes, *CRC Handbook of Chemistry and Physics*. CRC press, 2013.

[30] J. R. Paul, "The optical activity of glucose as influenced by normal and diabetic urine," *Journal of Clinical Investigation*, vol. 1, no. 4, p. 317, 1925.

[31] P. Dokic, J. Jakovljevic, and L. Dokic-Baucal, "Molecular characteristics of maltodextrins and rheological behaviour of diluted and concentrated solutions," *Colloids and Surfaces A: Physicochemical and Engineering Aspects*, vol. 141, no. 3, pp. 435–440, 1998.

[32] S. Alali, K. J. Aitken, A. Schröder, D. J. Bagli, and I. A. Vitkin, "Optical assessment of tissue anisotropy in ex vivo distended rat bladders," *Journal of biomedical optics*, vol. 17, no. 8, pp. 0 860 101–0 860 108, 2012.

[33] J. Peacock, *Astronomical Statistics*. The University of Edinburgh, 2012.

Glossary

Chirality Chirality a property of a molecule where it have different properties in different spatial orientations.

Fixed Pattern Noise This is intensity variations on the detector that are not temporally varying..

Intensity Observable value with which polarisation states are measured.

Intensity Error A deterministic source of variation on the ideal intensity measured by the detector.

Intensity Variations A type of influence on the system that varies the measured intensity from the ideal.

Irradiance The measure of power per unit area of a light wave. Typically in $\frac{W}{m^2}$.

Noise A stochastic source of variation on the ideal intensity measured by the detector, usually modelled with a probabilistic distribution.

Random Variable A variable that can undergo random variations in value.